Article

Neuron

Complementary Tuning of Na^+ and K^+ Channel Gating Underlies Fast and Energy-Efficient Action Potentials in GABAergic Interneuron Axons

Highlights

- Brief AP duration and high AP frequency in PV^+-BCs may imply high metabolic cost
- Energy for AP generation in PV^+-BC axons is only 1.6 times the theoretical minimum
- Fast Na_v inactivation and delayed Kv3 activation maximize AP energy efficiency
- Tuning of Na_v–Kv3 gating optimizes fast signaling and energetics in interneurons

Authors

Hua Hu, Fabian C. Roth, David Vandael, Peter Jonas

Correspondence

huah@medisin.uio.no (H.H.), peter.jonas@ist.ac.at (P.J.)

In Brief

Hu et al. demonstrate that action potentials in parvalbumin-expressing GABAergic interneuron axons are energetically efficient, which is highly unexpected given their brief duration. High energy efficiency emerges from the combination of fast inactivation of voltage-gated Na^+ channels and delayed activation of Kv3 channels in the axon.

Hu et al., 2018, Neuron *98*, 156–165
April 4, 2018
https://doi.org/10.1016/j.neuron.2018.02.024

CellPress

CellPress

Neuron
Article

Complementary Tuning of Na^+ and K^+ Channel Gating Underlies Fast and Energy-Efficient Action Potentials in GABAergic Interneuron Axons

Hua Hu,[1,2,*] Fabian C. Roth,[1] David Vandael,[2] and Peter Jonas[2,3,*]
[1]Division of Physiology, Department of Molecular Medicine, Institute of Basic Medical Sciences, University of Oslo, 0317 Oslo, Norway
[2]IST Austria (Institute of Science and Technology Austria), Am Campus 1, A-3400 Klosterneuburg, Austria
[3]Lead Contact
*Correspondence: huah@medisin.uio.no (H.H.), peter.jonas@ist.ac.at (P.J.)
https://doi.org/10.1016/j.neuron.2018.02.024

SUMMARY

Fast-spiking, parvalbumin-expressing GABAergic interneurons (PV^+-BCs) express a complex machinery of rapid signaling mechanisms, including specialized voltage-gated ion channels to generate brief action potentials (APs). However, short APs are associated with overlapping Na^+ and K^+ fluxes and are therefore energetically expensive. How the potentially vicious combination of high AP frequency and inefficient spike generation can be reconciled with limited energy supply is presently unclear. To address this question, we performed direct recordings from the PV^+-BC axon, the subcellular structure where active conductances for AP initiation and propagation are located. Surprisingly, the energy required for the AP was, on average, only ~1.6 times the theoretical minimum. High energy efficiency emerged from the combination of fast inactivation of Na^+ channels and delayed activation of Kv3-type K^+ channels, which minimized ion flux overlap during APs. Thus, the complementary tuning of axonal Na^+ and K^+ channel gating optimizes both fast signaling properties and metabolic efficiency.

INTRODUCTION

Fast-spiking, parvalbumin-expressing GABAergic interneurons (PV^+-BCs) play a key role in several higher microcircuit functions, such as feedforward and feedback inhibition, high-frequency network oscillations, and pattern separation. For all of these functions, the fast signaling properties of these neurons play a critical role (Hu et al., 2014). A functional hallmark of PV^+-BCs is the fast-spiking phenotype, i.e., the ability of the neurons to generate high-frequency trains of action potentials (APs) during sustained current injection *in vitro* (Rudy and McBain, 2001). A related property is the brief duration of the AP, referred to as "thin spike" in the classical literature (Mountcastle et al., 1969). Both functional properties are generated by the expression of specific types of voltage-gated ion channels, most importantly the selective expression of Kv3-type K^+ channels in these neurons (Rudy and McBain, 2001). Short APs generate a short refractory period and therefore allow PV^+-BCs to produce high-frequency activities under a variety of behavioral conditions *in vivo*, for example with a frequency of ~20 Hz during theta periods and ~120 Hz during sharp-wave ripples in the hippocampal CA1 region (Lapray et al., 2012; Gan et al., 2017). Short APs also generate a brief presynaptic Ca^{2+} current in presynaptic terminals (Bischofberger et al., 2002), and thereby trigger fast and temporally precise transmitter release at PV^+-BC output synapses (Goldberg et al., 2005). Thus, brief APs are key components of the repertoire of fast signaling mechanisms of PV^+-BCs.

AP generation in neurons is energetically expensive. Previous calculations suggested that up to 50% of the total energy budget of the brain is required for AP mechanisms (Attwell and Laughlin, 2001). In essence, Na^+ and K^+ ion fluxes during APs dissipate ion gradients, and the action of the Na^+/K^+ ATPase is required to re-establish these gradients. PV^+-BCs may require an excessively large amount of energy. First, PV^+-BCs generate spikes at a much higher frequency than principal neurons under *in vivo* conditions. Second, brief spikes are considered energetically expensive (Carter and Bean, 2009). Short APs are associated with large K^+ conductances in the repolarization phase, leading to overlapping Na^+ and K^+ fluxes in this period. As these counter-fluxes do not contribute to membrane potential changes, but need to be reversed by Na^+/K^+ ATPase activity, short APs are predicted to be energetically inefficient. Consistent with this prediction, the ratio of total Na^+ flux to the theoretical minimum, is substantially larger than 1 in several models of fast-spiking neurons (Wang and Buzsáki, 1996; Sengupta et al., 2010) and in direct measurements from cell bodies of GABAergic interneurons (Carter and Bean, 2009). The combination of fast-spiking activity and high-energy cost per spike in PV^+-BCs might be a major challenge for the brain's energy budget. However, these conclusions were based on the analysis of voltage-gated Na^+ channels in neuronal somata. Whether they hold in axons of PV^+-BCs, where >95% of Na^+ channels are located in this cell type (Hu and Jonas, 2014), remains an open question.

The energy efficiency of APs in axons of different cell types varies over a wide range (Table S1). In the squid giant axon and other invertebrate axons, the AP-related total Na^+ influx is ~4 times the theoretical minimum; thus, the AP is considered energetically inefficient in this type of axon (Hodgkin and Huxley,

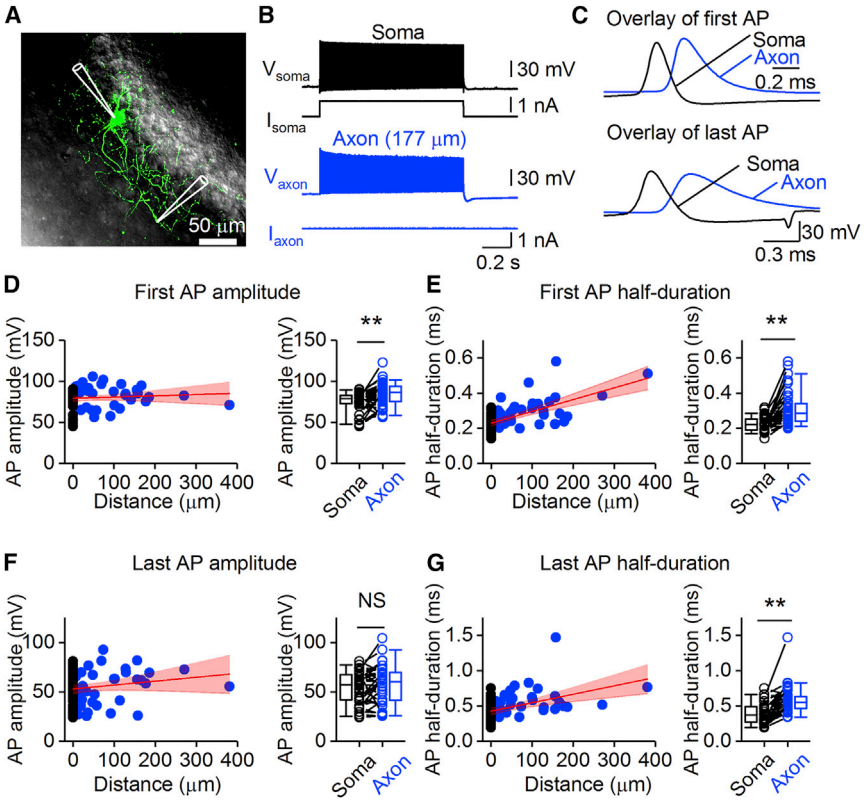

Figure 1. Brief APs in PV$^+$-BC Axons at Physiological Temperature

(A) Maximal confocal stack projection of a fast-spiking, parvalbumin-expressing BC in the dentate gyrus filled with Alexa Fluor 488 during the experiment. Recording pipettes are illustrated schematically.

(B) A simultaneous soma-axon recording of a high-frequency AP train in response to a 1 s depolarizing current pulse applied at the soma. Black traces, somatic voltage and corresponding current. Blue traces, axonal voltage and corresponding current (177 µm from the soma).

(C) First (top) and last (bottom) APs in the high-frequency train plotted at an expanded timescale. Data in (B) and (C) are from the same cell.

(D) Left: plot of AP peak amplitude against distance of the axonal recording site from the soma for the first AP in the high-frequency train. Data were fit with a linear function (red line, Spearman $\rho = 0.24$, $p = 0.04$). Red area represents 95% confidence interval. Black circles, data from 36 somatic recordings; blue circles, data from 36 axonal recordings. Right: summary graph of somatic and axonal AP peak amplitudes in 41 soma-axon recordings. Data points from the same experiment are connected by lines. Open circles, data from individual recordings; box chart, median value and distribution of all data points. **$p = 0.001$.

(E) Left: plot of AP half-duration against distance of the axonal recording site from the soma for the first AP. Data were fit with a linear function (red line, Spearman $\rho = 0.58$, $p < 0.0001$). Red area represents 95% confidence interval. Black circles, data from 36 somatic recordings; blue circles, data from 36 axonal recordings. Right: summary graph of somatic and axonal AP half-durations in 41 soma-axon recordings. Data points from the same experiment are connected by lines. Open circles, data from individual recordings; box chart, median value and distribution of all data points. **$p < 0.0001$.

(F) Similar to (D) but for the last AP in the high-frequency train. Spearman $\rho = 0.11$, $p = 0.36$. Data from 32 (left) and 36 (right) soma-axon recordings. NS indicates $p = 0.16$.

(G) Similar to (E) but for the last AP in the high-frequency train. Spearman $\rho = 0.53$, $p < 0.0001$. Data from 32 (left) and 36 soma-axon recordings (right). **$p < 0.0001$.

Whiskers in box charts indicate the 5th and 95th percentile of data points, and the box itself indicates median, first quartile, and third quartile of the data points.

1952; Hodgkin, 1975; Sengupta et al., 2010). In the axon of neocortical layer 5 pyramidal neurons, the Na^+ entry ratio is ~1.8–2.3 (Hallermann et al., 2012). In contrast, in hippocampal mossy fiber axons, the total Na^+ influx is only ~1.3 times the theoretical minimum; thus, the AP is considered energetically efficient (Alle et al., 2009). How the energy efficiency of APs in GABAergic interneuron axons compares to these values is, at present, unknown. To measure the energy efficiency of APs in PV$^+$-BCs, we made direct recordings from the axon of these neurons. We found that the energy efficiency of APs was higher than expected, approaching the value previously reported in hippocampal mossy fiber axons. Combined analysis of channel gating and modeling identified the combination of fast Na^+ channel inactivation and delayed activation of Kv3 channels as the key mechanism generating short, energy-efficient APs.

RESULTS

Short APs in PV$^+$-BC Axons at Physiological Temperature

To determine the relation between AP duration and energy efficiency of the AP, we first measured AP amplitude and half-duration in PV$^+$-BC axons (Figure 1). Recordings were performed at physiological temperature (34°C–37°C), because energy efficiency was previously reported to be temperature dependent (Yu et al., 2012). Axonal APs in PV$^+$-BC axons at physiological temperature showed an overshooting amplitude and a short duration (Figures 1D and 1E). For the first axonal AP in a high-frequency train, the median peak amplitude was 86.4 ± 2.2 mV, and the half-duration was 0.29 ± 0.02 ms. For the last axonal AP in a high-frequency train, the amplitude was 59.1 ± 3.2 mV, and the half-duration was 0.55 ± 0.03 ms (Figures 1F and 1G; Table S2). Detailed analysis of axonal and somatic APs revealed that the AP amplitude was slightly larger ($p < 0.01$ for the first AP, Figures 1D and 1F), and the half-duration was slightly longer in the axon than in the soma ($p < 0.01$ for both first and last AP, Figures 1E and 1G). In comparison to principal neurons (Kole et al., 2007; Geiger and Jonas, 2000), the somatic AP was substantially faster in PV$^+$-BCs (Kole et al., 2007), whereas the axonal AP waveforms were comparable in the two types of cells. These properties of the AP could contribute to the energy efficiency of the spike in PV$^+$-BC axons.

Energy-Efficient APs in PV$^+$-BC Axons

Next, we directly measured the energy efficiency of APs in PV$^+$-BC axons (Figures 2A–2F). APs were recorded in the

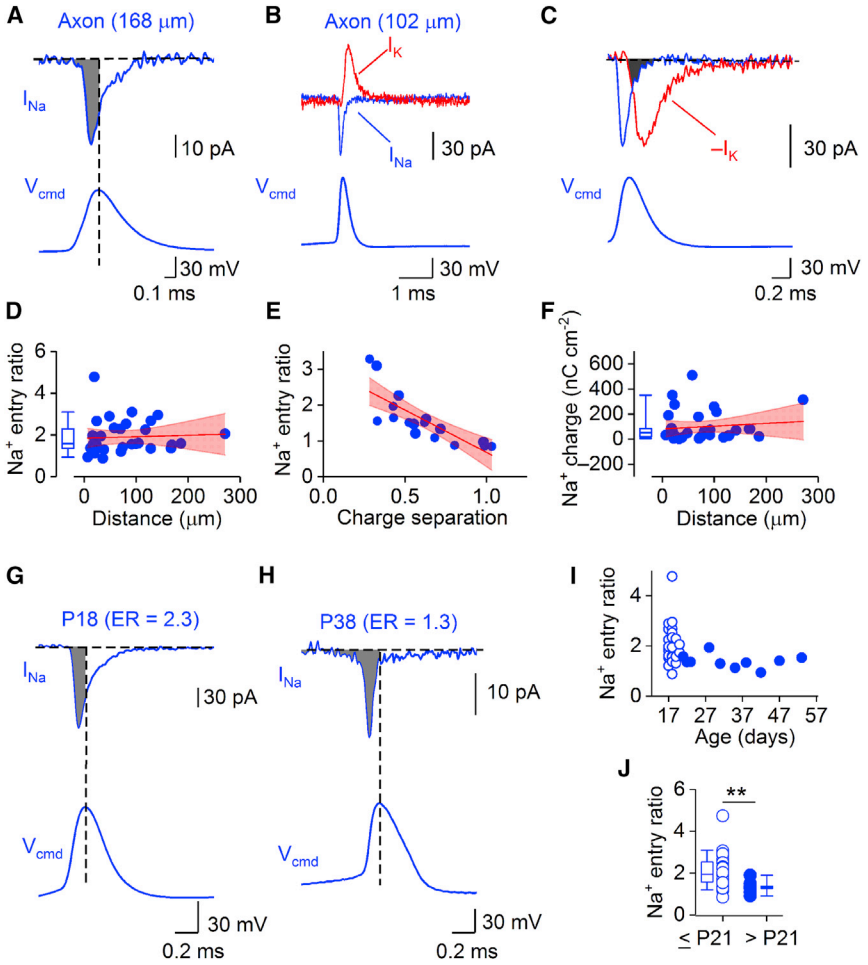

Figure 2. Energy-Efficient APs in PV^+-BC Axons

(A) Na^+ current (top) evoked by an AP waveform (bottom) in an outside-out patch excised from a PV^+-BC axon (168 μm from the soma). Filled gray area represents Na^+ entry before the AP peak.

(B) Na^+ and K^+ currents (top) evoked by an AP waveform (bottom) in an outside-out patch excised from a PV^+-BC axon (102 μm from the soma).

(C) Na^+ and K^+ currents in (B) shown at expanded scales. The K^+ current was inverted ($-I_K$) to illustrate the overlap of Na^+ and K^+ currents (filled gray area). Bottom traces in (A)–(C) indicate previously recorded AP applied as voltage-clamp command (V_{cmd}). Data in (B) and (C) are from the same recording.

(D) Left: box chart of Na^+ entry ratio (34 axonal recordings) in PV^+-BC axons. Right: plot of Na^+ entry ratio against distance from the soma in 31 axonal recordings. Red line represents a linear function fit to the data points (Spearman $\rho = 0.28$, $p = 0.13$).

(E) Plot of Na^+ entry ratio against Na^+-K^+ charge separation in 18 axonal recordings. Data were fit with a linear function (red line, Spearman $\rho = -0.92$, $p < 0.0001$).

(F) Left: box chart of Na^+ charge transfer (36 axonal recordings) in PV^+-BC axons. Right: plot of Na^+ charge transfer against distance from the soma (33 axonal recordings). Red line represents a linear function fit to the data points (Spearman $\rho = 0.08$, $p = 0.67$). In (D)–(F), blue circles represent data from individual recordings, and red area depicts 95% confidence interval.

(G) Na^+ current (top) evoked by an AP waveform (bottom) in an outside-out patch excised from a P18 PV^+-BC axon with a Na^+ entry ratio (ER) of 2.3. Filled gray area represents Na^+ entry before the AP peak.

(H) Similar to (G) but from a P38 PV^+-BC axon with an ER of 1.3.

(I) Summary plot of Na^+ entry ratio against postnatal age.

(J) Summary plot of Na^+ entry ratios in young (≤P21) and mature (>P21) PV^+-BC axons. Open circles in (I) and (J), data from 25 young (≤P21) PV^+-BC axons; filled circles, data from 9 mature (>P21) PV^+-BC axons; box chart, median value and distribution of all data points. **p = 0.002.

Whiskers in box charts indicate the 5th and 95th percentile of data points, and the box itself indicates median, first quartile, and third quartile of the data points.

axon and applied as voltage-clamp commands to subsequently excised outside-out patches (Figures 2A–2C). To quantify AP energetics, we used three previously established measures: the Na^+ entry ratio, the Na^+-K^+ charge separation, and the total charge transfer in comparison to the theoretical minimum (Figure S1) (Carter and Bean, 2009; Alle et al., 2009; Hallermann et al., 2012). In PV^+-BC axons, the median entry ratio for the first AP in a high-frequency train was 1.60 ± 0.13 (34 axonal recordings; Figure 2D) and the charge separation was 0.59 ± 0.06 (18 axonal recordings; Figure 2E). Entry ratio and charge separation in single cells were negatively correlated, suggesting that both quantities provided related information about energy efficiency (Figure 2E). The entry ratio was independent of distance of the axonal recording site from the soma (Figure 2D), and slightly decreased during repetitive stimulation (Figure S2). As the excitability of PV^+-BCs is known to mature during development (Doischer et al., 2008; Okaty et al., 2009; Goldberg et al., 2011), we further analyzed the dependence of the entry ratio on the age of the animals (Figures 2G–2J). Surprisingly, the entry ratio significantly declined as a function of age ($p = 0.002$), suggesting developmental maturation of energy efficiency.

Next, we computed the Na^+ charge transfer during single APs (Figure 2F). The median Na^+ charge density was 51.7 ± 19.6 nC cm^{-2} for the first AP. The Na^+ charge density was independent of distance (Figure 2F) and markedly decreased during repetitive firing (Figure S2). To compare the Na^+ charge transfer during an AP to the theoretical minimum of a pure capacitor (Alle et al., 2009; Carter and Bean, 2009), we computed Na^+ and K^+ conductance (g_{Na} and g_K) waveforms during APs at physiological temperature, dividing current by driving force at each time point (Figures 3A–3C). We inserted experimentally measured conductance waveforms into a passive cable model of an axon and coupled them to a threshold trigger mechanism (Alle et al., 2009; Figure 3D–3H; Method Details). We then estimated peak conductance densities by minimizing the sum of squared errors between measured and simulated APs. This approach allowed us to compare the Na^+ charge density with the product of

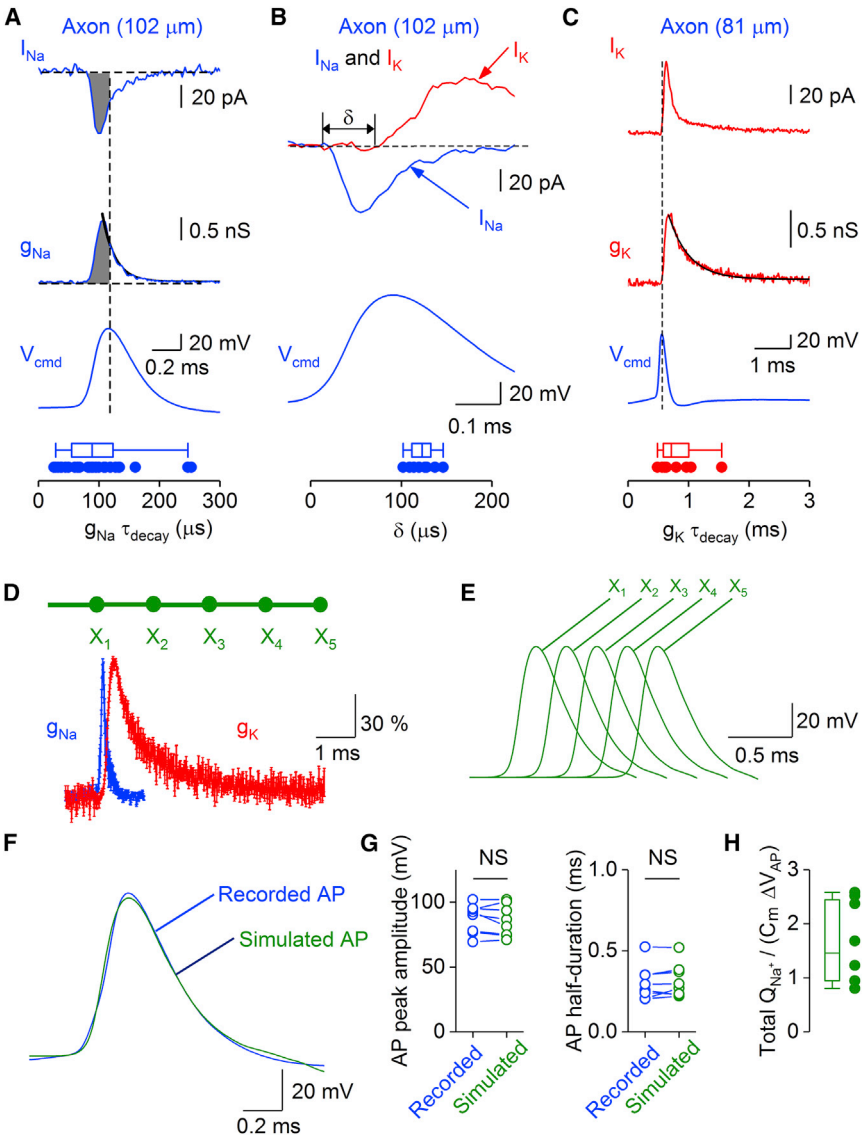

Figure 3. Complementary Tuning of Na^+ and K^+ Conductances Enhances AP Energy Efficiency in PV^+-BC Axons

(A) Top: Na^+ current (I_{Na}) and corresponding conductance (g_{Na}) evoked by an AP waveform in an axonal membrane patch 102 μm from the soma. Black line indicates a monoexponential function fit to the decay phase of g_{Na}. Bottom: summary graph of the g_{Na} decay time constant. Filled circles, individual data points in 28 axonal recordings, box chart indicates the median and distribution of data points.

(B) Top: Na^+ current (I_{Na}, blue) evoked by an AP waveform superimposed on the K^+ current (I_K, red) recorded from the same outside-out patch (102 μm from the soma) to illustrate the delay (δ) between the onset of Na^+ current and K^+ current. Bottom: summary graph of the delay. Filled circles, individual data points in 8 axonal recordings, box chart indicates the median and distribution of data points. Traces in (A) and (B) are from the same recording.

(C) Top: K^+ current (I_K) and corresponding conductance (g_K) evoked by an AP waveform in an axonal membrane patch (81 μm from the soma). Black line indicates a monoexponential function fit to the decay phase of g_K. Bottom: summary graph of the g_K decay time constant. Filled circles, individual data points in 8 axonal recordings, box chart indicates the median and distribution of data points.

(D) Simulation of APs in a hybrid model, in which experimentally determined conductance traces were introduced into a computational model by a threshold trigger mechanism (Alle et al., 2009). Top: structure of the axon cable used for simulations. For further model parameters, see Method Details. Bottom: plot of normalized g_{Na} and g_K versus time (average from 8 axonal recordings; error bars indicate SEM). Individual conductance values were normalized to peak value for each cell, averaged, and normalized to the peak of the average trace to account for slight differences in peak time.

(E) Propagation of the AP along the axon. Traces represent membrane potential at 5 equally spaced axonal sites. Note that the model predicts fast AP propagation.

(F) Overlay of experimentally recorded AP (blue) and simulated AP (green) in the center of the cable. Peak conductance values (g_{Na} and g_K) and threshold in the model were varied to provide the best fit to experimental observations. Both traces were vertically aligned by subtracting the membrane potential before the AP and horizontally aligned by subtracting the AP peak time. Weight factors for $t_{peak} - 250\ \mu s \leq t \leq t_{peak} + 500\ \mu s$ set to 1, and to 0.2 otherwise. Note that measured and simulated traces were in good agreement.

(G) Summary graph of AP peak amplitude (left) and half-duration (right). Note that the model accurately reproduced the experimental observations. Data points representing individual experimentally recorded APs and corresponding simulated APs were connected by lines. NS indicates p = 0.23 and 0.36, respectively.

(H) Summary graph of total Na^+ charge, relative to the theoretical minimum.

Whiskers in box charts indicate the 5th and 95th percentile of data points, and the box itself indicates median, first quartile, and third quartile of the data points.

specific capacitance (0.9 μF cm^{-2}) × AP amplitude (Alle et al., 2009). The ratio of ionic charge density to capacitive charge density was 1.46 ± 0.27 (8 axonal recordings). Thus, by all measures of energetics, APs in PV^+-BC axons were more energy efficient than expected from their brief duration. Energetic efficiency was higher than in squid axons (Hodgkin, 1975; Sengupta et al., 2010) and pyramidal neuron axons (Hallermann et al., 2012) and almost approached that in hippocampal mossy fiber axons (Alle et al., 2009).

Fast Na^+ Channel Inactivation and Delayed K^+ Channel Activation during APs

To determine the mechanisms underlying the energy efficiency of the AP in PV^+-BC axons, we examined the kinetic properties of g_{Na} and g_K during APs at physiological temperature (Figures 3A–3C). g_{Na} reached its peak during the AP upstroke and subsequently decayed with a time constant of 89 ± 11 μs (Figure 3A). In contrast, g_K rose with a significant delay. Consequently, the time difference between the onset of I_{Na} and I_K was 123 ± 5 μs

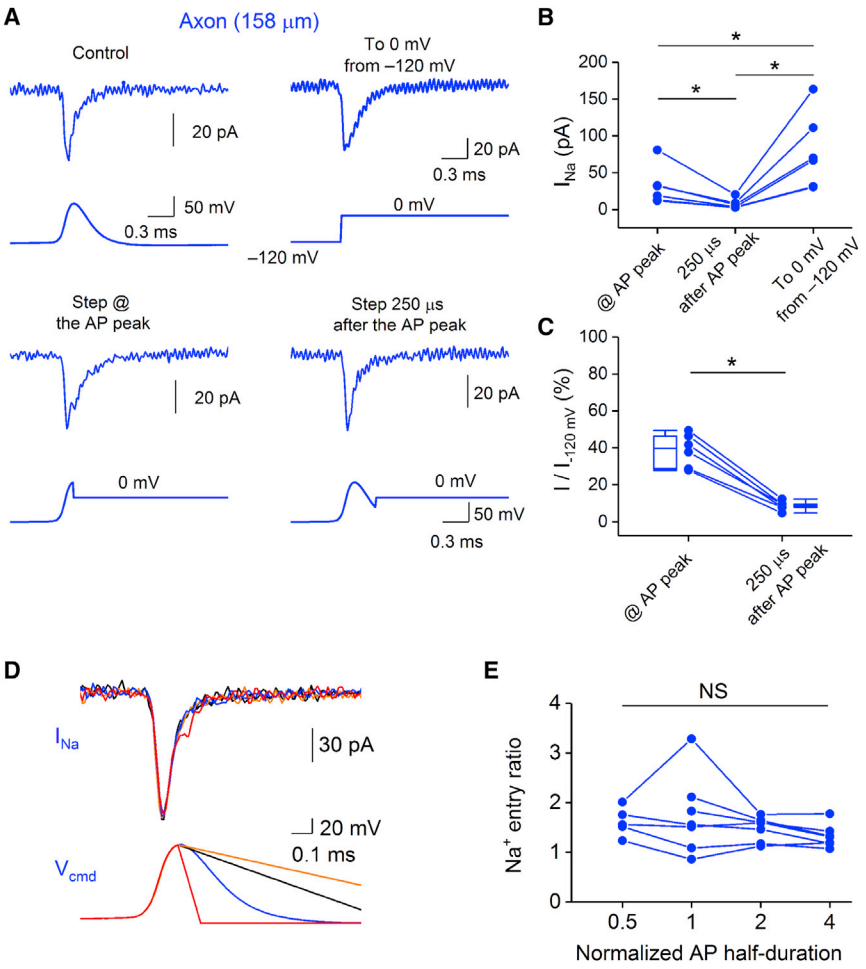

Figure 4. Rapid and Complete Na^+ Channel Inactivation during APs Promotes Energy Efficiency in PV^+-BC Axons

(A) Top: Na^+ currents evoked by an AP waveform (left) or a test pulse to 0 mV from a membrane potential of −120 mV (right) in an axonal outside-out patch (158 μm from the soma). Bottom: a test pulse to 0 mV was applied at the peak (left) or 250 μs after the peak (right) of the AP to determine the degree of Na^+ channel inactivation. All traces are from the same experiment.

(B) Summary graph showing the amplitude of Na^+ currents evoked by the test pulse applied at the peak or 250 μs after the peak of the AP waveform and that of the Na^+ current elicited by applying the test pulse from −120 mV. *p = 0.04.

(C) Summary graph showing the degree of Na^+ channel inactivation at the peak and 250 μs after the AP peak. Na^+ channel inactivation was quantified as the ratio (I/I_{-120mV}) of current amplitudes evoked by the test pulse applied at or after the AP peak to the maximal amplitude of the Na^+ current elicited by the test pulse applied from a membrane potential of −120 mV. Data from the same experiment were connected by lines. Box charts indicate the median value and distribution of all data points. *p = 0.04.

(D) Na^+ currents elicited by AP waveforms of different half-durations in an axonal outside-out patch. To systematically scale the half-duration of the AP waveform, we replaced the repolarization phase of the AP waveform with linear functions of different slope values. Each AP waveform and its corresponding Na^+ current trace were plotted in the same color.

(E) Summary graph showing the effects of changing AP half-duration on Na^+ entry ratio in 7 axonal recordings. Data from the same experiment were connected by lines. NS indicates p = 0.4. Whiskers in box charts indicate the 5th and 95th percentile of data points, and the box itself indicates median, first quartile, and third quartile of the data points.

(Figure 3B). Finally, g_K decayed with a time constant of 714 ± 124 μs (Figure 3C). Thus, the rapid decay of g_{Na} combined with the delayed rise of g_K minimized Na^+-K^+ charge overlap, enhancing the energy efficiency of the AP.

Which mechanisms contribute to the rapid g_{Na} decay? Na^+ channels may close by deactivation, inactivation, or a combination of these mechanisms (Raman and Bean, 1997; Carter and Bean, 2009). To distinguish between these possibilities, we applied test pulses to 0 mV at different time points after the AP peak (Figure 4A). Test pulses added 250 μs after the AP peak produced only minimal additional current, indicating that Na^+ channels were fully inactivated (Figures 4A–4C). Furthermore, we scaled the repolarization phase of AP voltage-clamp waveforms (Figures 4D and 4E). Broadened APs produced current responses that were nearly identical to those of short APs. Furthermore, control and broadened APs gave the same Na^+ entry ratio, indicating complete Na^+ channel inactivation. Thus, Na^+ inflow during axonal APs was terminated by Na^+ channel inactivation rather than deactivation. Taken together, fast inactivation of Na^+ channels and delayed activation of K^+ channels underlies the generation of short, highly energy-efficient APs in PV^+-BC axons. Additionally, fast deactivation of K^+ channels will facilitate repetitive high-frequency firing (Rudy and McBain, 2001).

Gating and Subcellular Distribution of Na^+ and K^+ Channels in PV^+-BC Axons

To reveal the biophysical mechanisms of energy-efficient APs in PV^+-BC axons, we characterized gating kinetics and channel distribution. For voltage-gated Na^+ channels, we analyzed steady-state activation and inactivation curves, activation and deactivation time constants, as well as inactivation onset and recovery time constants (see Hu and Jonas, 2014; Figure S3; Table S3). For voltage-gated K^+ channels, we measured steady-state activation curves, as well as activation and deactivation time constants (Figure S4; Table S4). High activation threshold, fast deactivation at negative membrane potentials, and sensitivity to 1 mM tetraethylammonium (TEA) indicated that g_K was primarily mediated by Kv3-type K^+ channels (Rudy and McBain, 2001; Bean, 2007). Comparison of Na^+ and K^+ channel gating revealed that Na^+ channel inactivation was

substantially faster than K^+ channel activation over a wide range of membrane potentials ($p = 0.041$ to 0.002 in the membrane potential range from −20 to 40 mV; Figure S3D versus Figure S4E), providing a biophysical explanation of the separation between g_{Na} and g_K during APs. Finally, we mapped the density of $\overline{g_{Na}}$ and $\overline{g_K}$ in PV^+-BC axons and compared them with those in the somata and dendrites (Figure S5). Whereas $\overline{g_{Na}}$ increased by more than 10 times along the dendritic-somatic-axonal axis (Hu and Jonas, 2014), $\overline{g_K}$ was more uniformly distributed (Figure S5B). Median $\overline{g_K}$ was 113.1 pS μm^{-2} in proximal axons, 145.1 pS μm^{-2} in distal axons, 115.9 pS μm^{-2} at the soma, and 80.0 pS μm^{-2} in dendrites. Thus, the $\overline{g_{Na}}$ to $\overline{g_K}$ ratio increased >10-fold along the dendrite-soma-axon axis (Figure S5E). The channel distribution in PV^+-BCs differed from that in pyramidal neurons, in which both Na^+ and K^+ channels were highly enriched in the axon initial segment (Kole et al., 2007) and density of A-type K^+ channels markedly increased as a function of distance in dendrites (Hoffman et al., 1997).

Energy-Efficient and Inefficient Regimes of Fast AP Generation in Models

With these detailed descriptions of channel kinetics and distribution in our hands, we performed computational modeling to analyze how the complex interplay between Na^+ and K^+ channel gating determined AP energy efficiency in PV^+-BC axons. First, we developed gating models of Na^+ and K^+ channels in PV^+-BC axons, which precisely captured our experimental observations (Hille, 2001; Figure S6). Next, we introduced these models into a single-compartment neuron to simulate the energy efficiency of the AP (Figure 5). For the standard values, the Na^+ entry ratio was 1.60, close to our experimental measurements. Finally, we varied Na^+ channel inactivation rates and $\overline{g_K}$ (the main determinants of AP duration) relative to standard values and generated contour plots of both AP half-duration and entry ratio against the two scaling factors (Figures 5A and 5B). When inactivation rates and $\overline{g_K}$ were varied by a factor of 0.3–3, the AP half-duration changed between 0.14 and 0.44 ms (Figure 5A). In parallel, the entry ratio varied between 1.2 and 4.8 (Figure 5B). Unexpectedly, changes in entry ratio and half-duration in the parameter space were largely orthogonal. Thus, a short AP duration was reached by combination of either fast Na^+ channel inactivation and low $\overline{g_K}$, or by combination of slow Na^+ channel inactivation and high $\overline{g_K}$ (Figures 5A and 5B). However, only the first regime was highly energy efficient, whereas the second regime was not. To explore the contribution of K^+ channel gating to energy efficiency, we further modified the K^+ channel properties (Figures 5C and 5D). Attenuating the characteristic gating properties of Kv3 channels, by either shifting the activation curve in the negative direction or abolishing the delay in activation, markedly increased the entry ratio, while accentuating these properties had opposite effects. Thus, the specific gating properties of Kv3 channels contribute to the energy efficiency of the AP in PV^+-BC axons.

Subcellular Allocation of Energy Efficiency in Detailed Active Models

Finally, we examined the subcellular distribution of energy efficiency of the AP in detailed active cable models of PV^+-BCs (Figures 5E–5G). In six fully reconstructed PV^+-BCs (Nörenberg et al., 2010), quantitative analyses revealed a characteristic pattern of AP energy efficiency at the subcellular level, with the local Na^+ entry ratio being substantially lower in the axon than in the dendrites (Figure 5F). However, the total Na^+ inflow showed an opposite subcellular location dependence, with 94.1% axonal contribution and 3.4% dendritic contribution (Figure 5F). Based on the results from detailed active cable models of PV^+-BCs, we were able to estimate the AP-related single-cell energy budget of these neurons. The total Na^+ inflow was 322 ± 90 × 10^6 Na^+ ions per single AP. With the known stoichiometry of the Na^+/K^+ ATPase (Rakowski et al., 1989), this corresponded to 107 ± 30 × 10^6 hydrolyzed ATP molecules per AP, with a major axonal and a minor dendritic signaling component (Figure 5G). Thus, the energy required per AP in a single PV^+-BC is substantially lower than in a layer 5 pyramidal neuron (400–800 × 10^6 ATP AP^{-1}; Hallermann et al., 2012).

DISCUSSION

It is widely thought that short APs, like those in GABAergic interneurons, are energetically inefficient. Our results change this view (Table S1). In comparison to invertebrate axons, energy efficiency (as judged by the total Na^+ charge divided by the theoretical minimum) was much higher than in squid axons (Hodgkin, 1975) or crab axons (Sengupta et al., 2010). In comparison to other mammalian axons, energy efficiency (as judged by Na^+ entry ratio) was higher than in pyramidal neuron axons (Hallermann et al., 2012). Remarkably, energy efficiency (as judged by total Na^+ charge over the theoretical minimum) came close to that in hippocampal mossy fiber axons (Alle et al., 2009). Finally, the total number of hydrolyzed ATP molecules per AP was substantially lower in PV^+-BCs than in layer 5 pyramidal neurons (Hallermann et al., 2012). Thus, by all measures, APs in PV^+-BCs were more energy efficient than previously thought.

AP Mechanisms in PV^+-BCs: Speed versus Energy Efficiency?

Short APs in axons make important contributions to the function of PV^+-BCs in microcircuits (Hu et al., 2014). Short APs are also important to minimize the refractory period following the AP (Rudy and McBain, 2001), a key requirement for the fast-spiking AP phenotype. Short APs also generate a brief presynaptic Ca^{2+} current in presynaptic terminals (Bischofberger et al., 2002), which, in turn, triggers fast and temporally precise transmitter release (Goldberg et al., 2005). Consequently, short APs contribute to both the ability of PV^+-BCs to generate high-frequency activity (Lapray et al., 2012) and fast, temporally precise transmission at interneuron output synapses (Gan et al., 2017).

It is generally thought that short APs are energetically inefficient (Carter and Bean, 2009). The simple rationale is that the short repolarization of these APs is associated with a high delayed rectifier K^+ conductance, which generates overlapping Na^+ and K^+ fluxes. However, our results demonstrate that the situation is mechanistically more complex. Our computational analysis based on realistic models of Na^+ and K^+ channel gating in PV^+-BC axons revealed that Na^+ entry ratio and half-duration can be dissociated. Short APs can be generated in regimes with

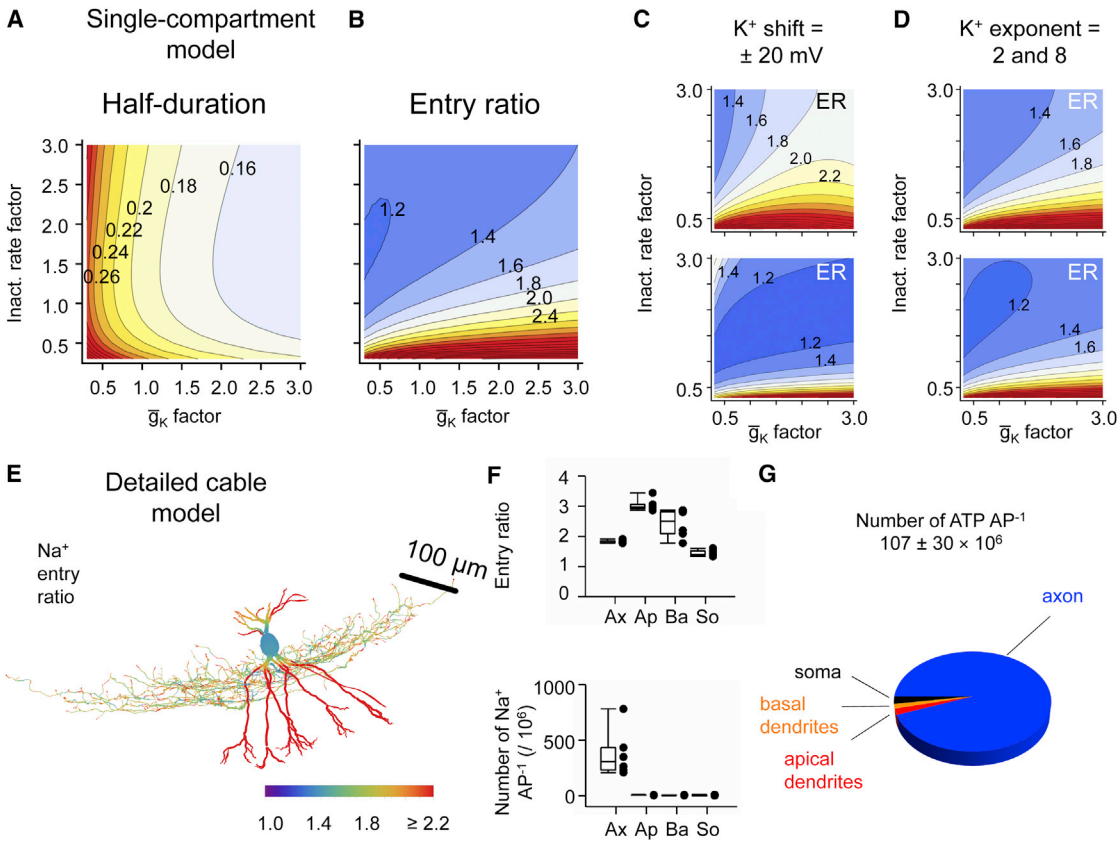

Figure 5. Matched Na^+ and K^+ Channel Gating Maximizes Energy Efficiency in PV^+-BC Axons

(A and B) Computational analysis of AP half-duration (A) and Na^+ entry ratio (B) in a single-compartment model as a function of scaling factors for Na^+ channel inactivation rates (ordinate) and maximal K^+ conductance (abscissa). Scaling factors of 1 correspond to the experimentally determined default values. Short APs can be generated with a wide range of Na^+ entry ratios. For model parameters, see Tables S5 and S6.

(C and D) Analysis of Na^+ entry ratio (ER) with altered K^+ channel gating. K^+ channel activation curves were shifted by 20 mV in the hyperpolarizing (C, top) or depolarizing (C, bottom) direction, and delayed rectifier properties were altered by reducing (from 4 to 2; D, top) or increasing (from 4 to 8; D, bottom) the exponent of K^+ channel activation. Note that both shift of the K^+ channel activation curve in the hyperpolarizing direction and reduction of the exponent of K^+ channel activation increased the Na^+ entry ratio, i.e., decreased the energy efficiency. Numbers near contour lines indicate half-duration values in ms (A) or Na^+ entry ratio values (B–D).

(E) Analysis of AP energetics in a detailed cable model of a dentate gyrus basket cell (BC2 from Nörenberg et al., 2010). Color code indicates Na^+ entry ratio; scale bar shown as inset. For model parameters, see Table S7. Note that the entry ratio is lower in the axon than in the dendrites, whereas the subcellular distribution of the total Na^+ charge is opposite, suggesting that subcellular structures with high Na^+ load show better optimized entry ratio. Ax, axon; Ap, apical dendrite; Ba, basal dendrite; So, soma.

(F) Box chart of entry ratio (top) and total Na^+ entry (bottom) in different subcellular compartments. Box charts indicate median and distribution of data points.

(G) Single-cell energy budget of PV^+-BCs (number of ATP per AP).

Whiskers in box charts indicate the 5th and 95th percentile of data points, and the box itself indicates median, first quartile, and third quartile of the data points.

fast Na^+ channel inactivation combined with small K^+ conductance or with slow Na^+ channel inactivation together with large K^+ conductance. PV^+-BC axons operate in the first regime, which is highly energy efficient.

Our results demonstrate that the energy efficiency of the AP in PV^+-BC axons is under developmental regulation. Previous work revealed that fast signaling properties of fast-spiking neurons mature during development, reflected by a shortening of the AP and an increase in the maximal AP frequency (Doischer et al., 2008; Okaty et al., 2009; Goldberg et al., 2011). Based on these findings, a developmental decrease of energy efficiency might have been expected. However, we found that energy efficiency slightly, but significantly, increased with age (Figures 2G–2J). These results corroborate the conclusion that short AP duration and high energy efficiency are not mutually exclusive, but can be correlated under specific conditions.

Reciprocal Tuning of Na^+ and K^+ Channel Gating Generates Fast, Energy-Efficient APs

Our results identify fast inactivation of voltage-gated Na^+ channels as a key mechanism underlying energy-efficient APs in PV^+-BC axons. Previous results demonstrated that inactivation of axonal Na^+ channels is ~2-fold faster than that of somatic channels in both hippocampal granule cells and PV^+-BCs (Engel and Jonas, 2005; Hu and Jonas, 2014). While fast Na^+ channel inactivation is expected to increase energy efficiency, it may

interfere with the fast-spiking AP phenotype. However, our results demonstrate that Na^+ channels in PV^+-BC axons also show a fast time course of recovery from inactivation (Figure S3; see Martina and Jonas, 1997). The combination of fast onset of inactivation and rapid recovery from inactivation guarantees energy efficiency during a spike, and at the same time ensures short refractory periods required for the fast-spiking AP phenotype.

In addition to fast Na^+ channel inactivation, the functional properties of voltage-gated K^+ channels contribute to energy efficiency. Both gating and pharmacological properties suggest that the K^+ channels expressed in PV^+-BC axons are mainly of the Kv3 type (Martina et al., 1998). Previous work demonstrated that fast deactivation and high activation threshold critically contribute to the fast-spiking AP phenotype of these neurons (Rudy and McBain, 2001; Bean, 2007). Our results indicate that the high activation threshold and, relatedly, the delayed activation of Kv3 channels in the overshoot phase of the AP play an important role in energy efficiency, providing a molecular mechanism for charge separation. Thus, the specific gating properties of Kv3 channels not only facilitate fast spiking, but also optimize the energy efficiency of the AP.

Our simulations reveal that a −20 mV shift of the Kv3 channel activation curve markedly decreases the energy efficiency of the AP in PV^+-BC axons (Figure 5C). Such a shift makes the channel activation curve almost Kv1-like (Table S4; Geiger and Jonas, 2000). Thus, our simulations suggest that the use of Kv3 channels for repolarization conveys higher energy efficiency than the use of Kv1 channels. Consistent with this simple idea, neocortical layer 5 pyramidal neuron axons exhibit a lower energy efficiency (Hallermann et al., 2012) and a larger Kv1-like conductance (Kole et al., 2007) than PV^+-BC axons. However, in apparent contrast with this possibility, mossy fiber axons show both high energy efficiency and large Kv1 conductance (Geiger and Jonas, 2000). Both the uniquely fast inactivation of Na^+ channels in mossy fiber axons (Engel and Jonas, 2005) and the preferential activation of Kv3 channels in Kv1/Kv3 channel mixtures by short APs (Alle et al., 2011) may explain this apparent discrepancy. Strategic subcellular distribution of Kv3, Kv1, and other K^+ channel types may further contribute to parallel optimization of function and energetic efficiency (Rowan et al., 2014).

Neuronal Polarity Contributes to Energy Saving

Our computational analysis further reveals that the marked polarity of PV^+-BCs, i.e., the steep gradient of Na^+ channel density along the dendrite-soma-axon axis, works as an energy-saving mechanism. In PV^+-BCs, the dendritic component of Na^+ influx and energy cost of the AP is only 3.4%, because voltage-gated Na^+ channels are largely absent from dendrites in these cells (Hu et al., 2010). In contrast, in thick-tufted layer 5 pyramidal neurons the dendritic contribution to the total Na^+ entry is ~30% (Hallermann et al., 2012). Limited excitability of dendrites of PV^+-BCs will save energy but restrict synaptic plasticity at glutamatergic input synapses, which often requires backpropagated APs (Mishra et al., 2016). Additionally, the absence of a region of high density of voltage-gated Na^+ channels in the axon initial segment in PV^+-BCs (Figure S5) may contribute to energy saving (Fleidervish et al., 2010; Hallermann et al., 2012). Finally, our computational results demonstrate a correlation between absolute Na^+ entry and energy efficiency, such that subcellular elements with the highest absolute Na^+ entry show the highest energetic efficiency. This is consistent with the hypothesis that energy consumption was an important factor in the optimization of PV^+-BC function during evolution.

Contribution of Fast-Spiking Cells to the AP Signaling-Related Energy Budget

The present results allow us to obtain improved estimates of the contribution of different cell types to the total energy budget required for AP signaling (Attwell and Laughlin, 2001; Buzsáki et al., 2007; Howarth et al., 2012). The proportion of PV^+ GABAergic interneurons has been estimated as 2.6% in the hippocampus (Bezaire and Soltesz, 2013) and 4.6% in the neocortex (estimated from the proportion of GABAergic interneurons, Meyer et al., 2011, and the percentage of PV^+ cells, Tremblay et al., 2016). However, the average firing frequency of PV^+-BCs *in vivo* is several-fold higher (~20 Hz; Lapray et al., 2012) than that of the principal neuron population (~1 Hz; Kowalski et al., 2016; Gentet et al., 2010). Using estimated ATP consumption values for PV^+-BCs (107×10^6 ATP per spike, this paper) and pyramidal neurons (400×10^6 ATP for tick-tufted layer 5 pyramidal cells; Hallermann et al., 2012), we calculate that the contribution of PV^+-BCs to the total energy consumption is ~14%–25%. If the energy efficiency of PV^+-BCs would be as high as that of hippocampal mossy fiber axons (entry ratio 1.26; Alle et al., 2009), this contribution would become slightly reduced, to ~11%–19%. However, if the energy efficiency was comparable to that of the squid giant axon (entry ratio 4; Hodgkin, 1975), this number would substantially rise to ~35%–62%. Thus, the optimization of the energy efficiency of single APs prevents PV^+-BCs from consuming a major fraction of the total AP-related energy budget.

Whether similar conclusions apply to fast-spiking neurons in other brain circuits remains to be determined. However, it is intriguing that other types of central axons in the mammalian CNS specialized on high-frequency coding also co-express fast-inactivating Na^+ channels and Kv3 channels (Leão et al., 2005; Ritzau-Jost et al., 2014). Thus, matched Na^+ and K^+ channel gating may represent a widely used design principle to implement metabolically efficient high-frequency coding schemes in the mammalian brain. Previous estimations suggested that low AP energy efficiency enforces low spike frequency and sparse coding in pyramidal neurons *in vivo* (Lennie, 2003). Following the same logic, our results imply that high AP energy efficiency contributes to the ability of GABAergic interneurons to generate high-frequency trains of spikes.

Our results may also shed light on the complex disease phenotype of Kv3 channelopathies (Kaczmarek and Zhang, 2017). Intriguingly, mutations in the Kv3.3 gene, which shift the activation curve in the hyperpolarizing direction, cause a neurodevelopmental-neurodegenerative disease phenotype, characterized by mild mental retardation and ataxia with early onset and slow progression (Waters et al., 2006). It is tempting to speculate that reduced AP energy efficiency, expected from left-shifted K^+ channel activation, contributes to the neurodegenerative component of the disease.

STAR★METHODS

Detailed methods are provided in the online version of this paper and include the following:

- KEY RESOURCES TABLE
- CONTACT FOR REAGENT AND RESOURCE SHARING
- EXPERIMENTAL MODEL AND SUBJECT DETAILS
- METHOD DETAILS
  - Axonal patch-clamp recording
  - Solutions and chemicals
  - Data analysis
  - Modeling of axonal Na^+ and K^+ channel gating
  - Computational models of AP energy efficiency and requirement in PV^+-BC axons
- QUANTIFICATION AND STATISTICAL ANALYSIS
  - Data and code availability

SUPPLEMENTAL INFORMATION

Supplemental Information includes six figures and seven tables and can be found with this article online at https://doi.org/10.1016/j.neuron.2018.02.024.

ACKNOWLEDGMENTS

We thank Drs. Thomas Klausberger and Arnd Roth for critically reading a previous manuscript version. We also thank Florian Marr for technical assistance, Eva Kramberger for editorial support, and Drs. Michael Hines and Ted Carnevale for useful suggestions. This project has received funding from the European Research Council (ERC) under the European Union's seventh framework programme, grant agreement number 268548 (to P.J.), under the European Union's Horizon 2020 research and innovation programme, grant agreement number 692692 (to P.J.), the Fond zur Förderung der Wissenschaftlichen Forschung (P 24909-B24; Z 312-B27, Wittgenstein award to P.J.), the Norwegian Research Council, grant agreement number 250866 (to H.H.), and the European Union's seventh framework programme (FP7-PEOPLE-2013-COFUND), grant agreement number 609020 -Scientia Fellows (to H.H. and F.C.R).

AUTHOR CONTRIBUTIONS

H.H., F.C.R., and D.V. performed experiments and analyzed data. P.J. performed modeling. H.H. and P.J. wrote the paper. All authors jointly revised the paper.

DECLARATION OF INTERESTS

The authors declare no competing interests.

Received: August 14, 2017
Revised: January 12, 2018
Accepted: February 23, 2018
Published: March 15, 2018

REFERENCES

Alle, H., Roth, A., and Geiger, J.R.P. (2009). Energy-efficient action potentials in hippocampal mossy fibers. Science *325*, 1405–1408.

Alle, H., Kubota, H., and Geiger, J.R.P. (2011). Sparse but highly efficient K_v3 outpace BK_{Ca} channels in action potential repolarization at hippocampal mossy fiber boutons. J. Neurosci. *31*, 8001–8012.

Attwell, D., and Laughlin, S.B. (2001). An energy budget for signaling in the grey matter of the brain. J. Cereb. Blood Flow Metab. *21*, 1133–1145.

Bean, B.P. (2007). The action potential in mammalian central neurons. Nat. Rev. Neurosci. *8*, 451–465.

Bezaire, M.J., and Soltesz, I. (2013). Quantitative assessment of CA1 local circuits: knowledge base for interneuron-pyramidal cell connectivity. Hippocampus *23*, 751–785.

Bischofberger, J., Geiger, J.R.P., and Jonas, P. (2002). Timing and efficacy of Ca^{2+} channel activation in hippocampal mossy fiber boutons. J. Neurosci. *22*, 10593–10602.

Buzsáki, G., Kaila, K., and Raichle, M. (2007). Inhibition and brain work. Neuron *56*, 771–783.

Carnevale, N.T., and Hines, M.L. (2006). The Neuron Book (Cambridge University Press).

Carter, B.C., and Bean, B.P. (2009). Sodium entry during action potentials of mammalian neurons: incomplete inactivation and reduced metabolic efficiency in fast-spiking neurons. Neuron *64*, 898–909.

Doischer, D., Hosp, J.A., Yanagawa, Y., Obata, K., Jonas, P., Vida, I., and Bartos, M. (2008). Postnatal differentiation of basket cells from slow to fast signaling devices. J. Neurosci. *28*, 12956–12968.

Engel, D., and Jonas, P. (2005). Presynaptic action potential amplification by voltage-gated Na^+ channels in hippocampal mossy fiber boutons. Neuron *45*, 405–417.

Fenwick, E.M., Marty, A., and Neher, E. (1982). Sodium and calcium channels in bovine chromaffin cells. J. Physiol. *331*, 599–635.

Fleidervish, I.A., Lasser-Ross, N., Gutnick, M.J., and Ross, W.N. (2010). Na^+ imaging reveals little difference in action potential-evoked Na^+ influx between axon and soma. Nat. Neurosci. *13*, 852–860.

Frankenhaeuser, B., and Moore, L.E. (1963). The effect of temperature on the sodium and potassium permeability changes in myelinated nerve fibres of Xenopus laevis. J. Physiol. *169*, 431–437.

Gan, J., Weng, S.M., Pernía-Andrade, A.J., Csicsvari, J., and Jonas, P. (2017). Phase-locked inhibition, but not excitation, underlies hippocampal ripple oscillations in awake mice in vivo. Neuron *93*, 308–314.

Geiger, J.R.P., and Jonas, P. (2000). Dynamic control of presynaptic Ca^{2+} inflow by fast-inactivating K^+ channels in hippocampal mossy fiber boutons. Neuron *28*, 927–939.

Gentet, L.J., Avermann, M., Matyas, F., Staiger, J.F., and Petersen, C.C. (2010). Membrane potential dynamics of GABAergic neurons in the barrel cortex of behaving mice. Neuron *65*, 422–435.

Goldberg, E.M., Watanabe, S., Chang, S.Y., Joho, R.H., Huang, Z.J., Leonard, C.S., and Rudy, B. (2005). Specific functions of synaptically localized potassium channels in synaptic transmission at the neocortical GABAergic fast-spiking cell synapse. J. Neurosci. *25*, 5230–5235.

Goldberg, E.M., Jeong, H.Y., Kruglikov, I., Tremblay, R., Lazarenko, R.M., and Rudy, B. (2011). Rapid developmental maturation of neocortical FS cell intrinsic excitability. Cereb. Cortex *21*, 666–682.

Guzman, S.J., Schlögl, A., and Schmidt-Hieber, C. (2014). Stimfit: quantifying electrophysiological data with Python. Front. Neuroinform. *8*, 16.

Halasy, K., and Somogyi, P. (1993). Subdivisions in the multiple GABAergic innervation of granule cells in the dentate gyrus of the rat hippocampus. Eur. J. Neurosci. *5*, 411–429.

Hallermann, S., de Kock, C.P., Stuart, G.J., and Kole, M.H. (2012). State and location dependence of action potential metabolic cost in cortical pyramidal neurons. Nat. Neurosci. *15*, 1007–1014.

Hille, B. (2001). Ion Channels of Excitable Membranes (Sinauer).

Hodgkin, A. (1975). The optimum density of sodium channels in an unmyelinated nerve. Philos. Trans. R. Soc. Lond. B Biol. Sci. *270*, 297–300.

Hodgkin, A.L., and Huxley, A.F. (1952). Currents carried by sodium and potassium ions through the membrane of the giant axon of *Loligo*. J. Physiol. *116*, 449–472.

Hoffman, D.A., Magee, J.C., Colbert, C.M., and Johnston, D. (1997). K^+ channel regulation of signal propagation in dendrites of hippocampal pyramidal neurons. Nature *387*, 869–875.

Howarth, C., Gleeson, P., and Attwell, D. (2012). Updated energy budgets for neural computation in the neocortex and cerebellum. J. Cereb. Blood Flow Metab. *32*, 1222–1232.

Hu, H., and Jonas, P. (2014). A supercritical density of Na^+ channels ensures fast signaling in GABAergic interneuron axons. Nat. Neurosci. *17*, 686–693.

Hu, H., Martina, M., and Jonas, P. (2010). Dendritic mechanisms underlying rapid synaptic activation of fast-spiking hippocampal interneurons. Science *327*, 52–58.

Hu, H., Gan, J., and Jonas, P. (2014). Interneurons. Fast-spiking, parvalbumin$^+$ GABAergic interneurons: from cellular design to microcircuit function. Science *345*, 1255263.

Kaczmarek, L.K., and Zhang, Y. (2017). Kv3 Channels: Enablers of rapid firing, neurotransmitter release, and neuronal endurance. Physiol. Rev. *97*, 1431–1468.

Kole, M.H., Letzkus, J.J., and Stuart, G.J. (2007). Axon initial segment Kv1 channels control axonal action potential waveform and synaptic efficacy. Neuron *55*, 633–647.

Kowalski, J., Gan, J., Jonas, P., and Pernía-Andrade, A.J. (2016). Intrinsic membrane properties determine hippocampal differential firing pattern in vivo in anesthetized rats. Hippocampus *26*, 668–682.

Lapray, D., Lasztoczi, B., Lagler, M., Viney, T.J., Katona, L., Valenti, O., Hartwich, K., Borhegyi, Z., Somogyi, P., and Klausberger, T. (2012). Behavior-dependent specialization of identified hippocampal interneurons. Nat. Neurosci. *15*, 1265–1271.

Leão, R.M., Kushmerick, C., Pinaud, R., Renden, R., Li, G.L., Taschenberger, H., Spirou, G., Levinson, S.R., and von Gersdorff, H. (2005). Presynaptic Na^+ channels: locus, development, and recovery from inactivation at a high-fidelity synapse. J. Neurosci. *25*, 3724–3738.

Lennie, P. (2003). The cost of cortical computation. Curr. Biol. *13*, 493–497.

Martina, M., and Jonas, P. (1997). Functional differences in Na^+ channel gating between fast-spiking interneurones and principal neurones of rat hippocampus. J. Physiol. *505*, 593–603.

Martina, M., Schultz, J.H., Ehmke, H., Monyer, H., and Jonas, P. (1998). Functional and molecular differences between voltage-gated K^+ channels of fast-spiking interneurons and pyramidal neurons of rat hippocampus. J. Neurosci. *18*, 8111–8125.

Meyer, H.S., Schwarz, D., Wimmer, V.C., Schmitt, A.C., Kerr, J.N.D., Sakmann, B., and Helmstaedter, M. (2011). Inhibitory interneurons in a cortical column form hot zones of inhibition in layers 2 and 5A. Proc. Natl. Acad. Sci. USA *108*, 16807–16812.

Micheva, K.D., Wolman, D., Mensh, B.D., Pax, E., Buchanan, J., Smith, S.J., and Bock, D.D. (2016). A large fraction of neocortical myelin ensheathes axons of local inhibitory neurons. eLife *5*, e15784.

Mishra, R.K., Kim, S., Guzman, S.J., and Jonas, P. (2016). Symmetric spike timing-dependent plasticity at CA3-CA3 synapses optimizes storage and recall in autoassociative networks. Nat. Commun. *7*, 11552.

Mountcastle, V.B., Talbot, W.H., Sakata, H., and Hyvärinen, J. (1969). Cortical neuronal mechanisms in flutter-vibration studied in unanesthetized monkeys. Neuronal periodicity and frequency discrimination. J. Neurophysiol. *32*, 452–484.

Nörenberg, A., Hu, H., Vida, I., Bartos, M., and Jonas, P. (2010). Distinct nonuniform cable properties optimize rapid and efficient activation of fast-spiking GABAergic interneurons. Proc. Natl. Acad. Sci. USA *107*, 894–899.

Okaty, B.W., Miller, M.N., Sugino, K., Hempel, C.M., and Nelson, S.B. (2009). Transcriptional and electrophysiological maturation of neocortical fast-spiking GABAergic interneurons. J. Neurosci. *29*, 7040–7052.

Rakowski, R.F., Gadsby, D.C., and De Weer, P. (1989). Stoichiometry and voltage dependence of the sodium pump in voltage-clamped, internally dialyzed squid giant axon. J. Gen. Physiol. *93*, 903–941.

Raman, I.M., and Bean, B.P. (1997). Resurgent sodium current and action potential formation in dissociated cerebellar Purkinje neurons. J. Neurosci. *17*, 4517–4526.

Ritzau-Jost, A., Delvendahl, I., Rings, A., Byczkowicz, N., Harada, H., Shigemoto, R., Hirrlinger, J., Eilers, J., and Hallermann, S. (2014). Ultrafast action potentials mediate kilohertz signaling at a central synapse. Neuron *84*, 152–163.

Rowan, M.J., Tranquil, E., and Christie, J.M. (2014). Distinct Kv channel subtypes contribute to differences in spike signaling properties in the axon initial segment and presynaptic boutons of cerebellar interneurons. J. Neurosci. *34*, 6611–6623.

Rudy, B., and McBain, C.J. (2001). Kv3 channels: voltage-gated K^+ channels designed for high-frequency repetitive firing. Trends Neurosci. *24*, 517–526.

Schwarz, J.R., and Eikhof, G. (1987). Na currents and action potentials in rat myelinated nerve fibres at 20 and 37°C. Pflugers Arch. *409*, 569–577.

Sengupta, B., Stemmler, M., Laughlin, S.B., and Niven, J.E. (2010). Action potential energy efficiency varies among neuron types in vertebrates and invertebrates. PLoS Comput. Biol. *6*, e1000840.

Shu, Y., Hasenstaub, A., Duque, A., Yu, Y., and McCormick, D.A. (2006). Modulation of intracortical synaptic potentials by presynaptic somatic membrane potential. Nature *441*, 761–765.

Tremblay, R., Lee, S., and Rudy, B. (2016). GABAergic interneurons in the neocortex: From cellular properties to circuits. Neuron *91*, 260–292.

Wang, X.J., and Buzsáki, G. (1996). Gamma oscillation by synaptic inhibition in a hippocampal interneuronal network model. J. Neurosci. *16*, 6402–6413.

Waters, M.F., Minassian, N.A., Stevanin, G., Figueroa, K.P., Bannister, J.P., Nolte, D., Mock, A.F., Evidente, V.G., Fee, D.B., Müller, U., et al. (2006). Mutations in voltage-gated potassium channel KCNC3 cause degenerative and developmental central nervous system phenotypes. Nat. Genet. *38*, 447–451.

Yu, Y., Hill, A.P., and McCormick, D.A. (2012). Warm body temperature facilitates energy efficient cortical action potentials. PLoS Comput. Biol. *8*, e1002456.

STAR★METHODS

KEY RESOURCES TABLE

REAGENT or RESOURCE	SOURCE	IDENTIFIER
Chemicals, Peptides, and Recombinant Proteins		
NaCl	VWR	27810.364
$NaHCO_3$	VWR	27778.293
KCl	VWR	26764.298
NaH_2PO_4	VWR	28013.264
D-glucose	VWR	101175P
Sucrose	VWR	27480.294
$MgCl_2$	VWR	25108.260
$CaCl_2$	VWR	22317.297
K-gluconate	Sigma-Aldrich	G4500
EGTA	Sigma-Aldrich	E4378
HEPES	Sigma-Aldrich	H3375
ATP	Sigma-Aldrich	A8937
$CdCl_2$	Sigma-Aldrich	208299
4-AP	Sigma-Aldrich	275875
TEA	Sigma-Aldrich	T2265
Alexa Fluor 488 hydrazide	Thermo Fisher Scientific	A10436
Experimental Models: Organisms/Strains		
Wistar rats	Charles River and Preclinical Facility, IST Austria	Strain code: 273
Software and Algorithms		
Igor Pro 6	Wavemetrics	V6.20–6.37
Fpulse	Ulrich Fröbe, University of Freiburg	3.19, 3.33
Stimfit	Guzman et al., 2014 (https://github.com/neurodroid/stimfit)	V0.9.2–0.13.2
Mathematica	Wolfram Research (http://www.wolfram.com/mathematica)	V11.0
NEURON	https://www.neuron.yale.edu/neuron/	V7.4
pClamp 9	Molecular Devices	V9.2.1.9
Origin	OriginLab	Origin 2015
ImageJ	https://imagej.nih.gov/ij/	V1.51j8
CorelDRAW	Corel Corporation	X8
Velocity	PerkinElmer	V5.5.1
Minitab	Minitab	V17

CONTACT FOR REAGENT AND RESOURCE SHARING

As Lead Contact, Peter Jonas is responsible for all reagent and resource requests. Please contact Peter Jonas (peter.jonas@ist.ac.at) with requests and inquiries.

EXPERIMENTAL MODEL AND SUBJECT DETAILS

Experiments on Wistar rats were approved by the Bundesministerium für Wissenschaft, Forschung und Wirtschaft (A. Haslinger, Vienna) and the responsible veterinarian at the University of Oslo, and were performed in strict accordance with institutional, national, and European guidelines for animal experimentation.

Recordings from axons of fast-spiking PV^+-BCs of the dentate gyrus in slices from 17- to 53-day-old Wistar rats of either sex were performed according to previously established experimental protocols (Hu and Jonas, 2014).

METHOD DETAILS

Axonal patch-clamp recording

Recordings from axons of fast-spiking PV^+-BCs of the dentate gyrus were performed according to previously established experimental protocols (Hu and Jonas, 2014). Transverse hippocampal slices (thickness 350 μm) were prepared from the brains of 17- to 53-day-old Wistar rats of either sex. Rats were maintained under light (7 am–7 pm) and dark cycle (7 pm–7 am) conditions and were kept in a litter of 8–10 animals together with the mother in a single cage. Slices were cut in ice-cold, sucrose-containing physiological extracellular solution using a vibratome (VT1200, Leica Microsystems), incubated in a maintenance chamber filled with standard physiological extracellular solution at ~34°C for 30 min, and subsequently stored at room temperature. Slices were then individually transferred into a recording chamber and superfused with standard physiological extracellular solution. For analysis of Na^+ and K^+ currents during APs, recordings were performed at near-physiological temperature (~35°C; range: 34–37°C), because the energy efficiency of the AP is known to be highly temperature-dependent (Yu et al., 2012). In these experiments, the bath solution was warmed by a resistive heating unit (Sigmann Elektronik, Hüffenhardt, Germany) prior to entering the recording chamber, and the recording temperature was continuously monitored with a micro thermistor positioned in the vicinity of the recorded neuron. For biophysical analysis of channel gating, recordings were made at room temperature (~24°C; range: 22–25°C) to maximize the precision of kinetic measurements. In each experiment, temperature was held constant within ± 0.5°C.

For recordings from interneuron axons, the following experimental strategy was used. First, a somatic recording was obtained, using an internal solution containing Alexa Fluor 488 (50 or 100 μM, Invitrogen). Second, after ~30 min of somatic whole-cell recording, the fluorescently labeled axon was tangentially traced from the PV^+-BC soma through the granule cell layer with a Nipkow spinning disk confocal microscope (Ultraview live cell imager, Perkin Elmer, equipped with an Orca camera, Hamamatsu and a solid-state laser, excitation wavelength 488 nm). Exposure time was minimized to avoid phototoxic damage. Finally, fluorescent and infrared differential interference contrast (IR-DIC) images were compared and axons were patched under IR-DIC. Recordings were made from either axon shafts or small spherical axon expansions, presumably representing "blebs" formed during the slicing procedure (Shu et al., 2006), at distances up to 418 μm from the soma. Axonal whole-cell recordings were readily obtained, consistent with minimal myelination in the dentate gyrus at the developmental stage used (Hu and Jonas, 2014; Halasy and Somogyi, 1993; Micheva et al., 2016). This procedure resulted in a simultaneous axon–soma recording configuration. From this configuration, axonal outside-out patches were obtained by slowly withdrawing the axonal pipette. In all cases, axons could be unequivocally distinguished from dendrites on the basis of smaller diameter, location within or adjacent to the granule cell layer, and abundance of tangential collaterals. As shown previously, AP properties and conductance values were similar between bleb and shaft recordings (Hu and Jonas, 2014). For documentation purposes, 6 cells were rescanned with a Leica TCS SP5 II confocal microscope (Leica Microsystems; Figure 1A).

Patch pipettes were fabricated from thick-walled borosilicate glass tubing (outer diameter: 2 mm, inner diameter: 1 mm) with a horizontal pipette puller (P-97, Sutter Instruments). When filled with internal solution, they had a resistance of 2–10 MΩ for somatic recording and 6–40 MΩ for axonal recording. Current- and voltage-clamp recordings were performed using a Multiclamp 700B amplifier (Molecular Devices). Series resistance was 15–90 MΩ. Cells with somatic resting potentials more positive than −50 mV were discarded. Pipette capacitance and series resistance compensation (bridge balance) were applied throughout current-clamp experiments. Bridge balance was monitored and readjusted as required. BCs were held at a membrane potential of ~−65 mV, injecting a holding current at the soma (range: −150 to +200 pA) or at the axon (range: −20 to −100 pA).

Signals were low-pass filtered at 10 kHz (or 4 kHz in a subset of experiments to measure g_K density, Figure S5), and sampled at 100 kHz with a CED power interface (Cambridge Electronic Design) or a Digidata 1322 converter board (Molecular Devices). Pulse protocols were generated using custom-made data acquisition software (FPulse versions 3.19 and 3.33, Ulrich Fröbe, University of Freiburg) running under Igor 6.20–6.37 (WaveMetrics) or pCLAMP 9 (Molecular Devices). To elicit Na^+ and K^+ currents that flow during APs, we applied an AP waveform that was previously recorded from the same axon (Figures 2, 3, and Figure S2) or a pre-recorded AP waveform from the axon of a different neuron (in a subset of recordings in Figure 2E and Figure 4) as the voltage-clamp command to the outside-out patch. Na^+ currents were pharmacologically isolated with 5–20 mM tetraethylammoniumchloride (TEA), 1–10 mM 4-aminopyrididine (4-AP), and 50–100 μM $CdCl_2$ added to the bath solution. To separate Na^+ and K^+ currents in the same axonal recording (Figures 2B, 2C, 2E, and 3B), we first recorded the total current in the presence of $CdCl_2$ and subsequently used TEA, 4-AP, and $CdCl_2$ to isolate the Na^+ current component. The K^+ current component was obtained by digital subtraction. The holding potential before and after the pulse sequence was −70 mV (Figures 2, 3, and 4 and Figure S2) or −90 mV (Figures S3–S5). In a subset of experiments in Figures 2E and 4, a 50-ms prepulse to −120 mV was applied to outside-out patches to remove Na^+ channel inactivation. Voltage protocols were applied to outside-out patches once every 3–15 s. Leak and capacitive currents were subtracted online using a 'P over −4' or 'P over −8' correction procedure.

PV^+-BCs were identified based on the non-accommodating, fast-spiking AP phenotype (average AP frequency > 50 Hz at room temperature and >150 Hz at physiological temperature in response to 1 s, 0.3- to 1-nA somatic current pulses), and the morphological properties of the axonal arbor, which was largely restricted to the granule cell layer and established basket-like structures around granule cell somata in confocal images. At ~35°C, the maximal AP frequency was 239 ± 8 Hz (range: 188–420 Hz, 46 cells, ≤2 nA current injection). In a subset of cells, identification was confirmed by post hoc biocytin labeling. In a previous sample of fast-spiking interneurons in the dentate gyrus analyzed in detail by light microscopy, the fast-spiking AP phenotype

was tightly correlated with the expression of parvalbumin (Hu et al., 2010). Furthermore, 78 of 83 cells were classical basket cells with tangential axon collaterals and basket-like branches around granule cell somata, whereas 5 out of 83 were axo-axonic cells with radial axon collaterals (Hu et al., 2010). Based on these results, the recorded cells in the present study were termed PV^+-BCs throughout.

Solutions and chemicals

The standard physiological extracellular solution contained 125 mM NaCl, 25 mM $NaHCO_3$, 3.5 mM KCl, 1.25 mM NaH_2PO_4, 2 mM $CaCl_2$, 1 mM $MgCl_2$, and 25 mM D-glucose (equilibrated with 95% O_2 and 5% CO_2 gas mixture). In experiments to determine Na^+ channel gating properties and K^+ channel density (Figures S3 and S5), the extracellular KCl concentration was reduced to 2.5 mM. For tail current measurements (Figures S4A–S4E), we raised the extracellular KCl concentration to 25 mM and reduced the concentration of NaCl to 102.5 mM accordingly.

The intracellular solution contained 120 mM K-gluconate, 20 mM KCl, 10 mM EGTA, 2 mM $MgCl_2$, 2 mM Na_2ATP, 10 mM HEPES, and 0%–0.2% biocytin, pH adjusted to 7.3 with KOH. 50–100 μM Alexa Fluor 488 (Invitrogen) was added to the internal solution for all somatic recording electrodes.

Data analysis

Analysis was performed using Stimfit 0.9.2–0.13.2 (Guzman et al., 2014), Clampfit 9 (Molecular Devices), Origin 2015 (Microcal), Excel (Microsoft), and Minitab 17 (Minitab). AP amplitude was measured from threshold (50 V s^{-1}), and half-duration was defined as the width of the AP at its half-maximal amplitude. To determine the AP metabolic efficiency, we used three different previously established quantities: Na^+ entry ratio, Na^+-K^+ charge separation, and total Na^+ charge in comparison to the theoretical minimum (Figure S1). The Na^+ entry ratio was calculated by dividing the total Na^+ charge during the AP by the Na^+ charge before the AP peak (Figure S1A) (Carter and Bean, 2009; Hallermann et al., 2012). To account for the delay caused by the 10 kHz external filter and the lag introduced by uncompensated series resistance (Carter and Bean, 2009), current traces were shifted by 58 μs with respect to the voltage-clamp waveform. This time-lag value was determined from the latency between the onset of the test pulse and the time point of half-maximal rise of tail currents during the deactivation protocol (Bischofberger et al., 2002). The charge separation was calculated by dividing the non-overlapping Na^+ charge by the total Na^+ charge during APs (Alle et al., 2009; Figure S1B). This parameter quantifies the overlap of Na^+ influx and K^+ efflux, during which the effects of these opposing currents on membrane potential cancel out. Only Na^+ currents with an amplitude exceeding five times the standard deviation of the background noise (0.5–2.0 pA) were included in the analysis of Na^+ entry ratio and charge separation.

Finally, we determined the total Na^+ influx relative to the theoretical capacitive minimum, using an approach similar to that developed by Alle et al. (2009) (Figures 3D–3H). APs were simulated in a hybrid model, in which experimentally measured conductance traces were inserted into a passive cable model by a threshold trigger mechanism (ModelDB accession number 135838). Conductance values during an AP were determined from the respective Na^+ and K^+ currents, normalized to the maximum, and temporally aligned so that the onset of the Na^+ conductance corresponded to t = 0. The onset point was measured as the intersection of a line through the 20 and 80% amplitude points of the rising phase with the baseline. Experimentally determined g_{Na} and g_K traces were filtered with a sliding window (±three sample points) and incorporated into Neuron mod files. Simulations were performed using NEURON 7.4 (Carnevale and Hines, 2006). Conductances were inserted into a simplified cylindrical axon (diameter 0.9 μm, total length 910 μm), in which 5 boutons (diameter 2 μm) were added equidistantly in an *en passant* manner (Engel and Jonas, 2005; Alle et al., 2009; Hu and Jonas, 2014). Conductances were activated when membrane potential at a given location exceeded a threshold value. To initiate APs, a current pulse was applied to one end of the axon. The three parameters of the model, Na^+ peak conductance, K^+ peak conductance, and activation threshold (range: −60 to −45 mV), were then varied until the sum of squared differences between simulated AP at the center bouton and measured AP were minimal. Finally, energy efficiency was calculated as the ratio of the Na^+ charge $Q_{Na} = \int I_{Na}(t)\,dt$ over the product $C_m \times \Delta V$, where I_{Na} is the Na^+ current, C_m is the specific membrane capacitance (0.9 μF cm^{-2}, Table S6, Nörenberg et al., 2010) and ΔV is the peak amplitude of the AP (Alle et al., 2009). AP amplitude was measured from threshold (50 V s^{-1}) rather than baseline, because our axonal recording sites were relatively proximal; consequently, the AP was preceded by an axonal depolarization reflecting somatic current injection.

The K^+ channel activation curve was obtained by plotting the peak amplitude of tail currents elicited by stepping to −130 mV after a voltage pulse against the absolute value of the voltage pulse, and data points were normalized to the maximal value in each experiment. The activation curve was fit with a Boltzmann function $f = 1 / (1+\mathrm{Exp}[(V_{1/2} - V)/k])$, where V is the membrane potential, $V_{1/2}$ is the midpoint potential, and k is the slope factor. K^+ current activation time constant was obtained by fitting the rising phase of the K^+ current with a function of the form $I(t) = a \times (1 - \mathrm{Exp}[-(t - \delta)/\tau])$ for $t > \delta$ and $I(t) = 0$ for $t \leq \delta$, where δ is a delay, τ is activation time constant, and a is the amplitude value. K^+ current deactivation time constant was obtained by fitting the decay phase of K^+ tail currents with a single exponential function. To plot conductance density against distance (Figure S5), $\overline{g_{Na}}$ was calculated based on the peak current at 0 mV and a maximal Na^+ channel open probability of 0.66 at this membrane potential (Hu and Jonas, 2014), assuming an Na^+ current reversal potential of 70 mV (Martina and Jonas, 1997). $\overline{g_K}$ was calculated from the steady-state current amplitude at 70 mV, assuming a maximal K^+ channel open probability of 1 at 70 mV, and a K^+ current reversal potential −95 mV (Martina et al., 1998).

Modeling of axonal Na^+ and K^+ channel gating

To determine the effects of Na^+ and K^+ channel gating on energy efficiency, we fit the experimental voltage-clamp data with models of Na^+ and K^+ channel gating (Hodgkin and Huxley, 1952; Hille, 2001; Engel and Jonas, 2005). For Na^+ channels, the total dataset consisted of activation curve, steady-state inactivation curve, activation time constant, activation delay, deactivation time constant, onset of inactivation, and recovery from inactivation. For K^+ channels, the full dataset was comprised of activation curve, activation time constant, activation delay, and deactivation time constant. Steady-state values of gating parameters were calculated as $x_\infty = \alpha_x / (\alpha_x + \beta_x)$, and time constants were computed as $\tau_x = 1 / (\alpha_x + \beta_x)$, where x = m, h, n, or n'. For fitting of steady-state activation and inactivation curves, $m_\infty{}^3$, $n_\infty{}^3$ n'_∞, and h were compared against the measured values. Similarly, for fitting the inactivation time constants, τ_h was compared against the experimental values. For fitting of activation and deactivation time constants, Na^+ or K^+ currents were simulated as $m(t)^3$ or $n(t)^3$ n'(t), with $x(t) = x_\infty - (x_\infty - x_0)\,\mathrm{Exp}(-t/\tau_x)$, with x = m or n. Simulated traces were then fit with an exponential function including (activation) or not including a delay (deactivation). The sum of squares of differences between experimental observations and model predictions was minimized using FindMinimum of Mathematica 11 (Wolfram Research) running under Windows 7. Weight factors were approximately set according to the inverse of squared standard errors of the data points.

The forward and backward rate constants were determined as:

$$\alpha_m(V) = A\,[-(V+B)]/\{\mathrm{Exp}[-(V+B)/C] - 1\} \quad \text{(Eq. 1a)}$$

$$\beta_m(V) = A(V+B)/\{\mathrm{Exp}[(V+B)/C] - 1\} \quad \text{(Eq. 1b)}$$

$$\alpha_h(V) = A\,\mathrm{Exp}(-V/C) \quad \text{(Eq. 2a)}$$

$$\beta_h(V) = A/\{\mathrm{Exp}[(-V+B)/C] + 1\}\,, \quad \text{(Eq. 2b)}$$

where V is membrane potential. The Na^+ conductance was calculated as $\overline{g_{Na}}$ x m^3 x h (Table S5).

To accurately describe the K^+ channel gating, simple Hodgkin-Huxley equations were inadequate. We therefore adopted a more complex model with two sets of rates:

$$\alpha_n(V) = A[-(V+B)]/\{\mathrm{Exp}[-(V+B)/C] - 1\} \quad \text{(Eq. 3a)}$$

$$\beta_n(V) = A\,\mathrm{Exp}(-V/C) \quad \text{(Eq. 3b)}$$

$$\alpha'_n(V) = A[-(V+B)]/\{\mathrm{Exp}[(-V+B)/C] - 1\} \quad \text{(Eq. 4a)}$$

$$\beta'_n(V) = A\,\mathrm{Exp}(-V/C), \quad \text{(Eq. 4b)}$$

where the K^+ conductance was calculated as $\overline{g_K}$ x n^3 x n' (Table S5).

Computational models of AP energy efficiency and requirement in PV^+-BC axons

To model the energy efficiency of the AP, we first used a single-compartment model (Table S6) (Wang and Buzsáki, 1996). $\overline{g_{Na}}$ was set to 500 pS μm^{-2} and $\overline{g_K}$ to 150 pS μm^{-2}, consistent with the experimental observations. To account for the differences in the recording temperature in voltage-clamp and current-clamp recordings, rates α_x and β_x were scaled assuming a 11.5°C temperature difference and Q_{10} values of 2.2, 2.9, and 3.0 for x = m, h, and n or n' (Schwarz and Eikhof, 1987; Frankenhaeuser and Moore, 1963). The equilibrium potentials for Na^+ and K^+ ions were assumed as +55 mV and −90 mV, respectively. The voltage dependence of Na^+ channel gating was shifted by 20 mV toward positive potentials to account for differences in the Donnan potential between whole-cell and isolated patch configuration (Fenwick et al., 1982) and time- and temperature-dependent shifts of activation and inactivation curves. Na^+ entry ratio was calculated as the total Na^+ charge over its fraction before the peak of the AP (Alle et al., 2009; Carter and Bean, 2009). To minimize effects of stimulation on the entry ratio, APs were initiated by setting the initial condition V(t = 0) to a value above AP voltage threshold.

To determine the energy efficiency in different subcellular compartments, we further used detailed cable models of BCs (Table S7). Simulations were performed using NEURON 7.4 (Carnevale and Hines, 2006) in combination with Mathematica. Detailed passive cable models of BCs taken from the previously published sample of Nörenberg et al., 2010 (cell 2, and other cells from the sample as indicated; ModelDB accession number 140789). Neurons had been filled with biocytin during recording, stained with

3,3′-diaminobenzidine, and fully reconstructed (including soma, dendrites, and entire axon) using a Neurolucida reconstruction system, as described in the previous publication (Nörenberg et al., 2010). The specific cable parameters were chosen according to approximate average values (Nörenberg et al., 2010). The integration time step was set to 1 or 5 μs. To convey maximal accuracy, the number of segments per section (nseg) was determined according to the "d-lambda rule" as nseg = L / (0.03 $\lambda_{1\ kHz}$), where L is the length of the section and $\lambda_{1\ kHz}$ is the alternating current length constant at 1 kHz. Na^+ and K^+ channels were inserted using the experimentally derived Na^+ and K^+ channel models. $\overline{g_{Na}}$ was set to 500 pS μm^{-2} in the axon, 200 pS μm^{-2} at the soma, and 50 pS μm^{-2} at the dendrite. $\overline{g_K}$ was uniformly set to 300 pS μm^{-2} in all compartments. The reversal potential of the leak conductance was chosen as −70 mV. APs were evoked by brief current pulses at the soma (2–4 nA, 1 ms). Subcellular analysis of Na^+ entry ratio revealed that the entry ratio was higher in the dendrites, but lower at the soma in comparison to the axon (Figure 5E). The higher dendritic entry ratio was expected for a passively propagated signal (Hallermann et al., 2012). In contrast, the lower somatic entry ratio was explained by the presence of the stimulus electrode at this site, as revealed by shifting the stimulation site from the soma into the proximal axon (unpublished observations).

QUANTIFICATION AND STATISTICAL ANALYSIS

Membrane potentials are specified without correction for liquid junction potentials. Values indicate median value ± standard error (SEM) unless stated otherwise. Whiskers in box charts indicate the 5th and 95th percentile of data points, and the box itself indicates median, first quartile, and third quartile of the data points. Significance of difference between two groups of data was assessed by a two-sided nonparametric Wilcoxon signed rank test or Wilcoxon rank sum test. For comparison among multiple groups, we used nonparametric Friedman or Kruskal-Wallis tests. Differences were considered significant if $p < 0.05$. Correlation between two variables was assessed with the nonparametric Spearman rank correlation test. Distances were measured from the point of origin of the axon to the axonal recording site along the axonal trajectory in the confocal maximal intensity stack projection, in which sections at different focal planes had been merged following each experiment. In five recordings, the axon could not be traced back from the recording site to the soma. These recordings were excluded from the analyses of distance-dependence. Conductance density values were calculated from conductance values using the previously established relation between patch area and pipette resistance (Hu and Jonas, 2014), requiring recalculation for previous dendritic measurements (Hu et al., 2010).

Data and code availability

Original data and programs were stored in the scientific repositories of the Institute of Science and Technology Austria and the University of Oslo and are available on request.

Neuron, Volume *98*

Supplemental Information

Complementary Tuning of Na^+ and K^+ Channel Gating Underlies Fast and Energy-Efficient Action Potentials in GABAergic Interneuron Axons

Hua Hu, Fabian C. Roth, David Vandael, and Peter Jonas

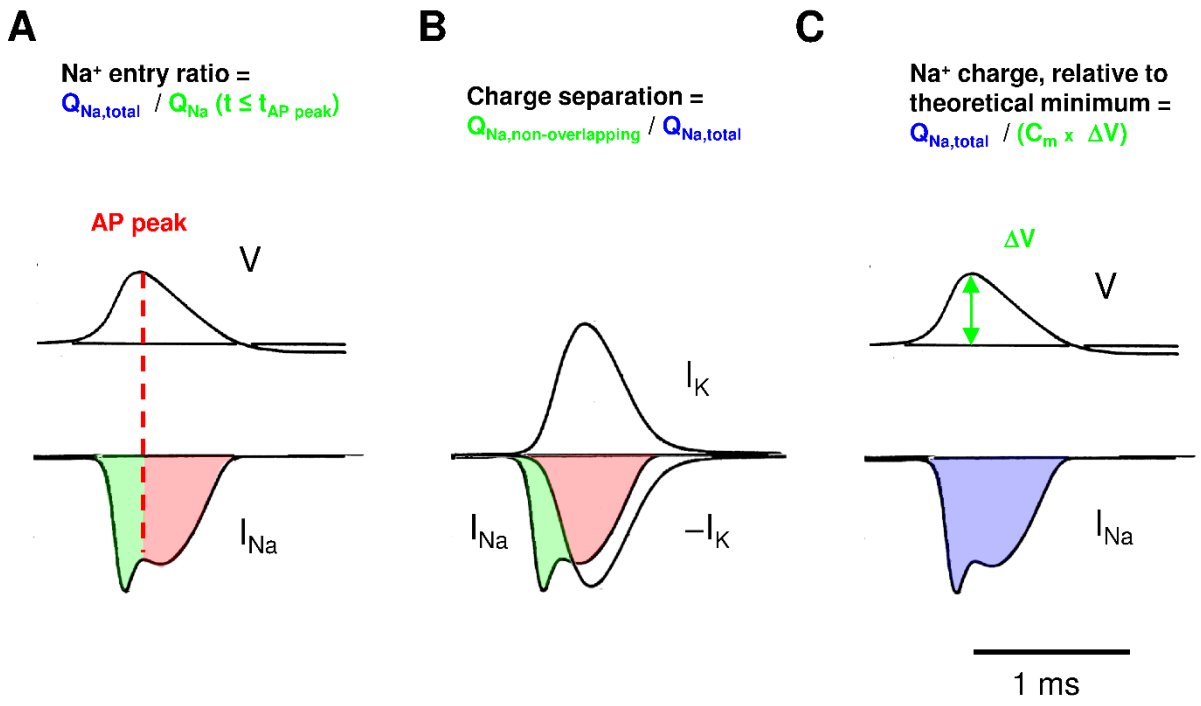

Figure S1. Definition of three different measures of energy efficiency of APs, related to Figures 1–4.

(**A**) Na^+ entry ratio (Hallermann et al., 2012). Vertical red line indicates the time of the peak of the AP. Green, Na^+ charge before AP peak; red, Na^+ charge after AP peak.

(**B**) Na^+-K^+ charge separation (Alle et al., 2009). Green, non-overlapping component; red, overlapping component of Na^+ current.

(**C**) Total Na^+ charge, relative to the theoretical minimum (Alle et al., 2009; Carter and Bean, 2009). Blue, value obtained by integration of Na^+ current. V indicates voltage, I_{Na} and I_K represent sodium and potassium currents during an AP. $-I_K$ depicts inverted potassium current, used to illustrate current overlap. Traces were taken from simulations of propagated APs in squid giant axon (Hodgkin and Huxley, 1952).

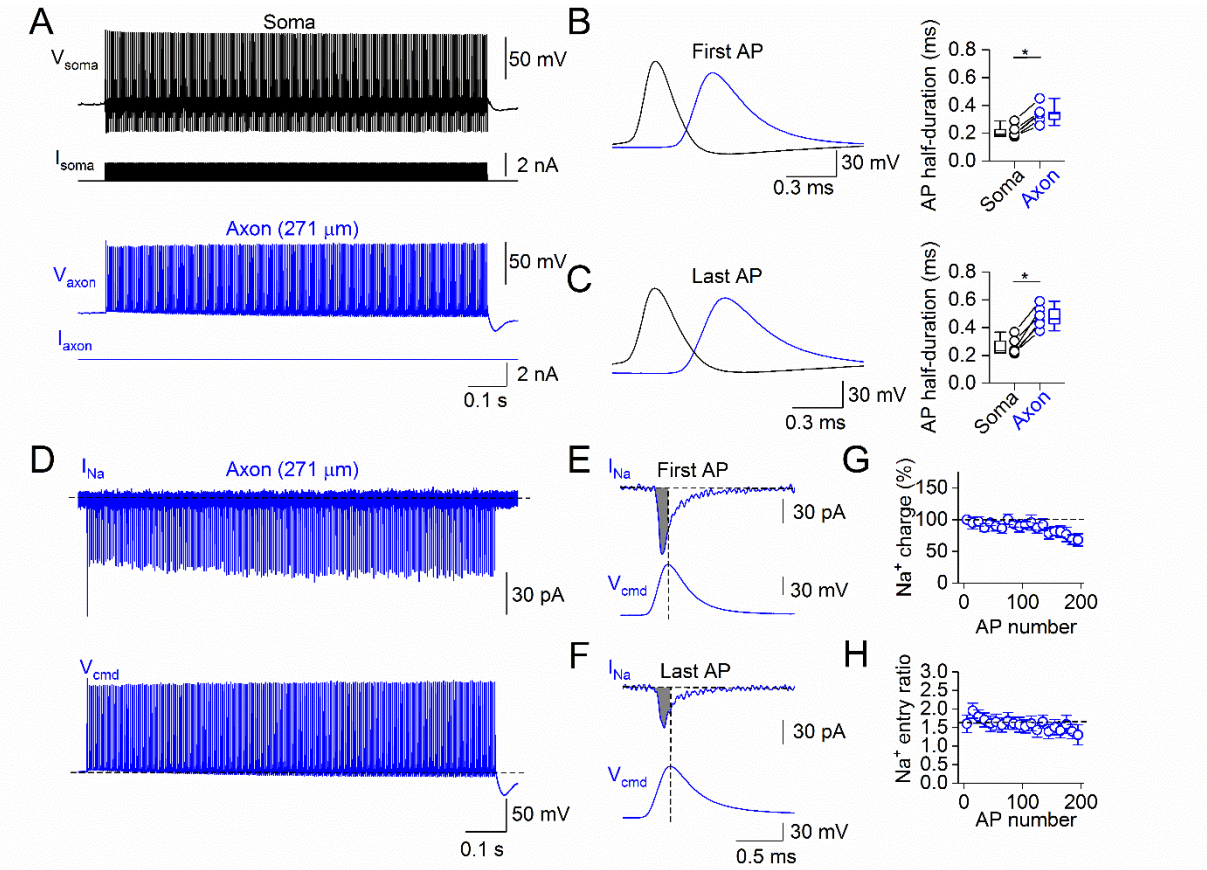

Figure S2. Activity-dependence of Na^+ entry during repetitive high-frequency firing, related to Figures 1 and 2.

(**A**) A simultaneous soma–axon recording from a PV^+-BC during somatic injection of a high-frequency train of short current pulses (200 stimuli at 200 Hz; 2 ms, 1.5 nA). Black traces, somatic voltage and corresponding current; blue traces, axonal voltage and corresponding current (271 µm from the soma).

(**B**) Left, overlay of somatic and axonal membrane potentials during the first AP in the train. Right, summary graph depicts first somatic and axonal AP half-durations in the 200-Hz train. Open circles, data from individual recordings. Somatic and axonal data points from the same experiment were connected by lines. Whiskers in box charts indicate the 5th and 95th percentile of data points, and the box itself indicates median, first quartile, and third quartile of the data points. * indicates P = 0.04

(**C**) Similar to (B), but for the last AP in the 200-Hz train. * indicates P = 0.04.

(**D**) Na^+ current (top) elicited by the 200-Hz AP train waveform (bottom) in the outside-out patch excised from a PV^+-BC axon (271 µm from the soma).

(**E, F**) Na^+ currents (top) elicited by the first (E) and last (F) APs (bottom) in the 200-Hz train shown at expanded scales. Filled gray area represents Na^+ entry before the AP peak.

Data in (A)–(F) are from the same cell.

(**G**) Plot of Na^+ charge transfer during the 200-Hz AP trains against AP number in 6 axonal recordings. Values in (G) normalized to those of the first AP in the train.

(**H**) Plot of Na^+ entry ratio during the 200-Hz AP trains against AP number in 6 axonal recordings. Each data point in (G) and (H) represents the mean value of 10 consecutive APs in the 200-Hz train.

Values in (G) and (H) are presented as mean ± SEM.

Recordings were performed at ~35°C.

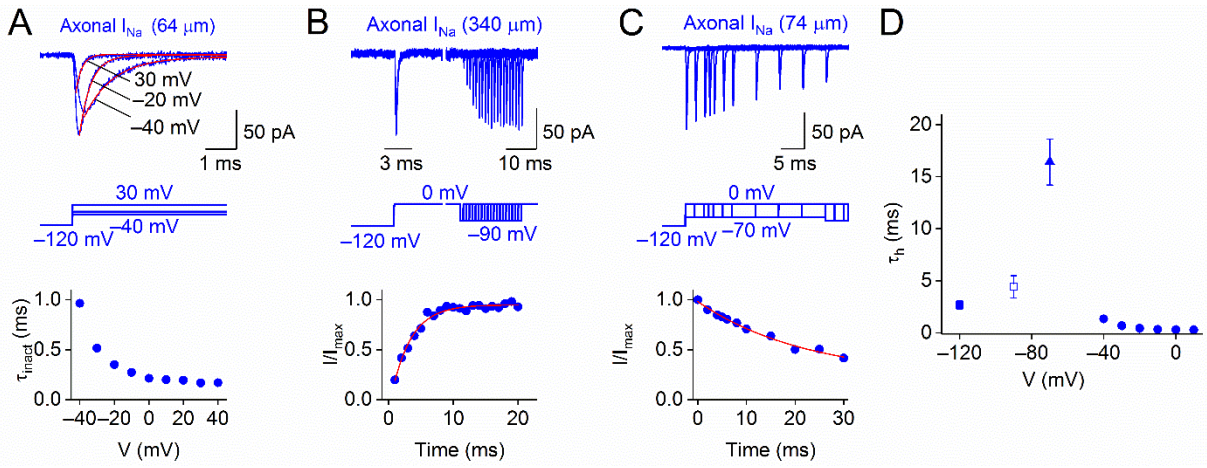

Figure S3. Rapid inactivation kinetics of Na^+ channels in PV^+-BC axons, related to Figures 2–4.

(**A**) Top, Na^+ currents and corresponding voltage pulses in an outside-out patch excised from a PV^+-BC axon (64 µm from the soma). Red lines represent monoexponential functions fit to the decay of the recorded traces. Bottom, plot of Na^+ channel inactivation time constant against voltage in the same recording. Data in (A) are replotted from Figure S6 in Hu and Jonas, 2014.

(**B**) Top, Na^+ currents and corresponding voltage pulses in an outside-out patch excised from a PV^+-BC axon (340 µm from the soma), demonstrating the fast time course of Na^+ current recovery from inactivation at −90 mV. Bottom, plot of Na^+ current peak amplitude against the duration of the interpulse interval at −90 mV in the same recording. The time constant of Na^+ channel recovery from inactivation was obtained by fitting the data points with a monoexponential function with an offset (τ = 3.0 ms, red line).

(**C**) Top, Na^+ currents and corresponding voltage pulses in an outside-out patch excised from a PV^+-BC axon (74 µm from the soma), demonstrating the time course of onset of Na^+ channel inactivation at −70 mV. Bottom, plot of Na^+ current peak amplitude against the duration of the conditioning pulse at −70 mV in the same recording. The time constant of onset of Na^+ channel inactivation was obtained by fitting the data points with a monoexponential function with an offset (τ = 22.5 ms, red line).

(**D**) Time constants of Na^+ current inactivation (filled circles, 11 axonal recordings), onset of inactivation at −70 mV (filled triangle, 7 axonal recordings), recovery from inactivation at −90 mV (open square, 3 axonal recordings) and recovery at −120 mV (filled square, 5 axonal recordings) plotted against voltage. For onset of inactivation at

−70 mV and recovery from inactivation at −90 mV or −120 mV, mean values were obtained by fit of average data, whereas SEM values were obtained from fits of data from individual experiments.

Values are presented as mean ± SEM. Recordings were obtained at ~24°C.

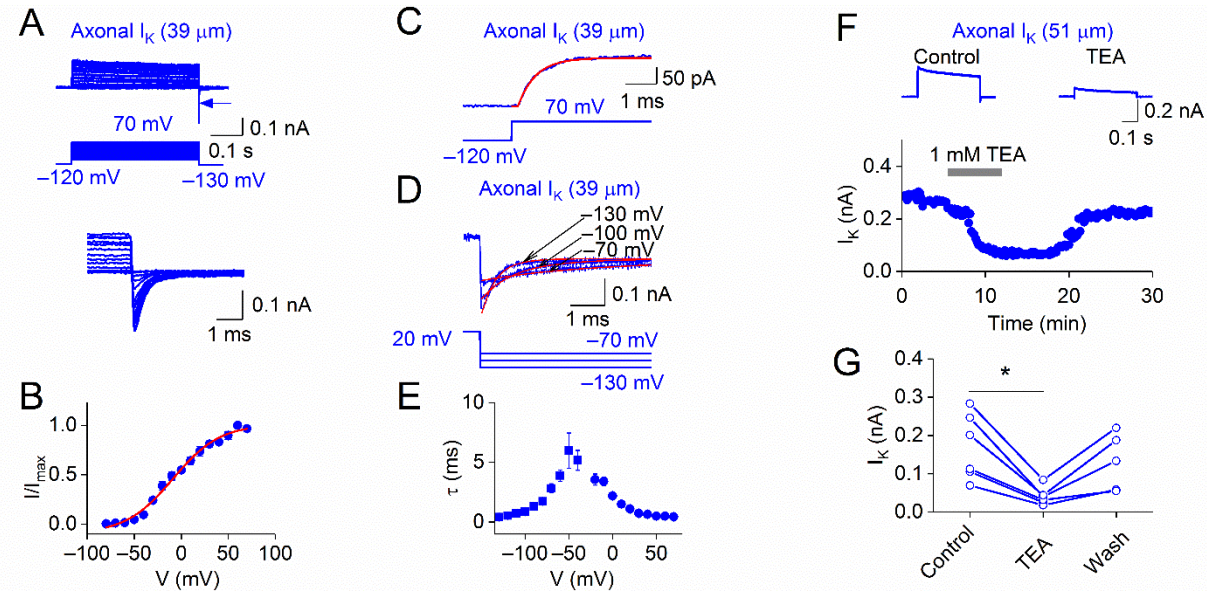

Figure S4. Gating and pharmacological properties of K⁺ channels in PV⁺-BC axons, related to Figures 2–4.

(**A**) Top, K⁺ currents in an outside-out patch excised from a PV⁺-BC axon 39 µm from the soma. The corresponding pulse protocol with increasing test pulse amplitude is shown in the center. Arrow indicates K⁺ tail currents at −130 mV, which were plotted at expanded scales at the bottom.

(**B**) Steady-state K⁺ current activation curve in PV⁺-BC axons. K⁺ current amplitudes were measured from tail currents at −130 mV and normalized to the maximal value in each experiment. Red line represents a Boltzmann function fit to the data points (5 axonal recordings).

(**C**) Top, onset of K⁺ current and corresponding voltage pulses in an outside-out patch excised from a PV⁺-BC axon (39 µm from the soma). Red lines represent a monoexponential function with delay fit to the current trace.

(**D**) K⁺ tail currents and the corresponding deactivation pulse protocol in an outside-out patch excised from a PV⁺-BC axon (39 µm from the soma). Red lines represent monoexponential functions fit to the tail currents. Data in (A), (C), and (D) were obtained from the same recording.

(**E**) Time constants of K⁺ current activation (filled circles, 5 axonal recordings) and deactivation (filled squares, 5 axon recordings) plotted against voltage.

(**F**) Top, K^+ currents in an axonal membrane patch excised 51 µm from the soma before and during bath application of 1 mM TEA. Bottom, steady-state K^+ current amplitude plotted against experimental time during the TEA application.

(**G**) Summary plot of steady-state K^+ current amplitude before, during, and after the application of TEA in 6 axonal patches. Data from the same experiment were connected by lines. * indicates P = 0.04.

Values in (B) and (E) are presented as mean ± SEM. Recordings were obtained at ~24°C.

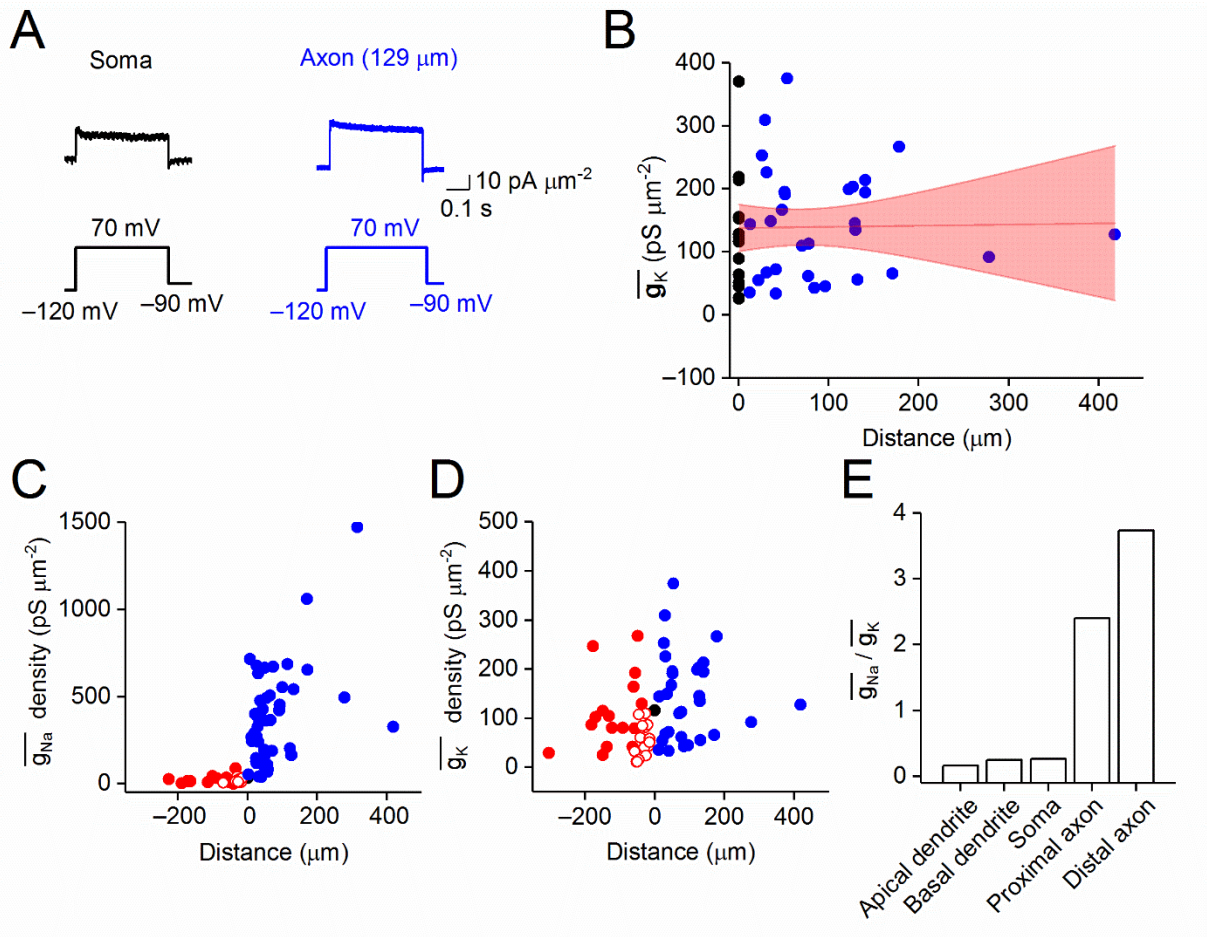

Figure S5. A steep subcellular gradient of Na^+ to K^+ conductance ratio in PV^+-BCs, related to Figures 2 and 3.

(**A**) Density of K^+ current in outside-out patches from the soma and the axon (129 µm from the soma). Black traces, somatic current density and corresponding voltage; blue traces, axonal current density and corresponding voltage. The current density was obtained dividing the current by the estimated patch area.

(**B**) K^+ conductance density plotted against distance from the soma. Black circles, data from 11 somatic recordings; blue circles, data from 30 axonal recordings. Data were fit with a linear function (red line, Spearman ρ = 0.42, P = 0.13). Red area represents 95% confidence interval.

(**C**) Summary plot of distance dependence of subcellular $\overline{g_{Na}}$ density in PV^+-BCs. Filled red circles, 15 apical dendritic patches; open red circles, 9 basal dendritic patches; filled black circle, median of 41 somatic patches; filled blue circles, 37 proximal (< 100 µm) and 11 distal (≥ 100 µm) axonal patches. Axonal data points were taken from Hu and Jonas, 2014.

(**D**) Summary plot of distance dependence of subcellular $\overline{g_K}$ density in PV$^+$-BCs. Filled red circles, 17 apical dendritic patches; open red circles, 14 basal dendritic patches; filled black circle, median of 11 somatic patches; filled blue circles, 19 proximal (< 100 µm) and 11 distal (≥ 100 µm) axonal patches. In (C) and (D), positive distances indicate axon, while negative distances represent dendrites.

(**E**) A steep subcellular gradient of Na^+ to K^+ conductance ratio in PV$^+$-BCs. To calculate the Na^+ to K^+ conductance ratio in each subcellular compartment, the median $\overline{g_{Na}}$ density was divided by the corresponding median $\overline{g_K}$ density.

Recordings were obtained at ~24°C.

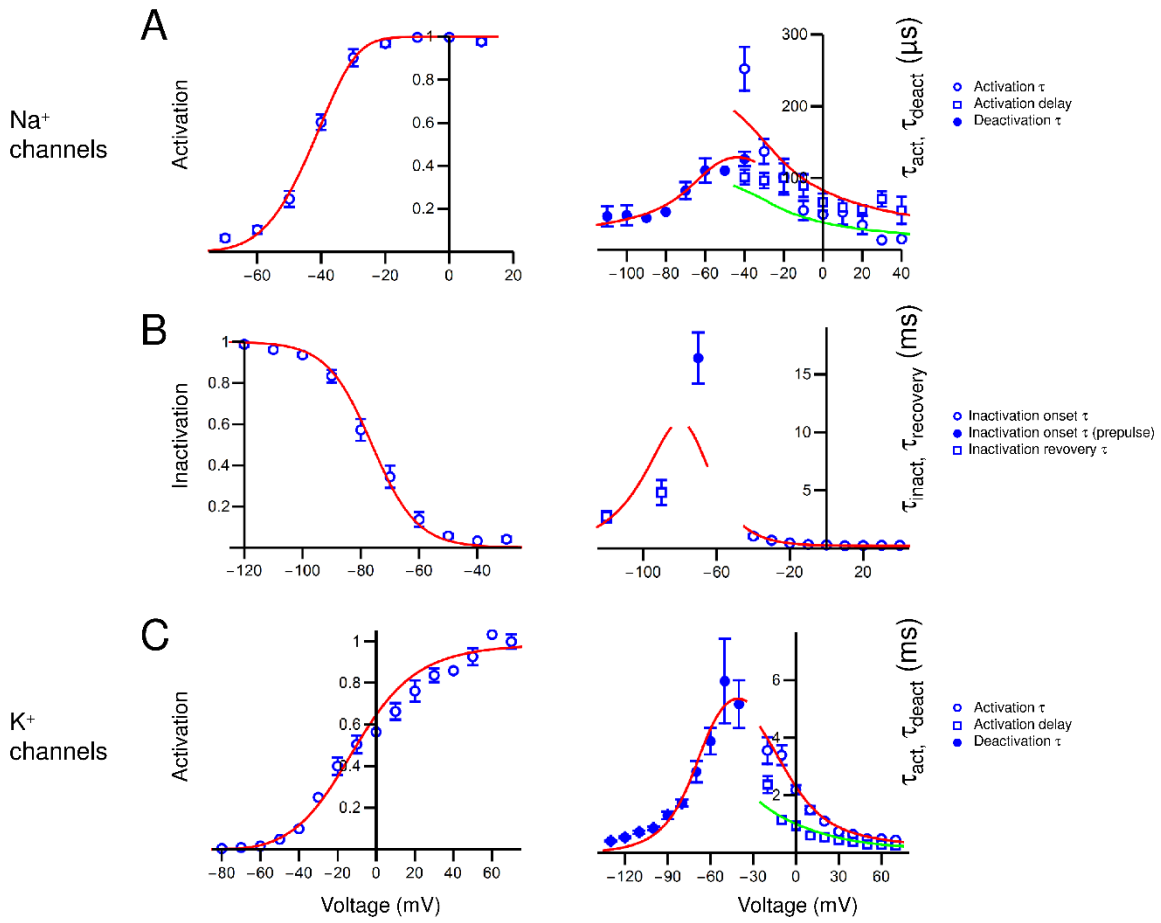

Figure S6. Experimentally constrained models of Na^+ and K^+ channels in PV^+-BC axons, related to Figures 2–4.

(**A**) Modeling of Na^+ channel activation. Left, Na^+ channel activation curve; right, activation time constants, delay, and deactivation time constants.

(**B**) Modeling of Na^+ channel inactivation. Left, steady-state inactivation curve; right, time constants of inactivation onset and recovery.

(**C**) Modeling of K^+ channel activation. Left, K^+ channel activation curve; right, activation time constants, delay, and deactivation time constants. Continuous curves in left plots indicate model predictions for activation and inactivation curves. Continuous curves in right plots indicate model predictions for time constants (red) and delay (green). For model parameters, see Table S5.

Values are presented as mean ± SEM.

Table S1. Comparison of energy efficiency measures in PV^+-BC axons with those in other types of axons, related to Figures 1–5.

Axon	Na^+ entry ratio	Charge separation	Total Na^+ charge / theoretical minimum	Total ATP consumption AP^{-1}	Reference
PV^+-BC axon	1.60 ± 0.13	0.59 ± 0.06	1.46 ± 0.27	107 ± 30 × 10^6	This paper
Squid axon			~4		Hodgkin, 1975; Sengupta et al., 2010
Crab axon			3.43		Sengupta et al., 2010
Mossy fiber axon		0.80 ± 0.02	1.26		Alle et al., 2009
Layer 5 pyramidal neuron axon	2.28 ± 0.16; 1.8 ± 0.2	0.63 ± 0.03		400–800 × 10^6	Hallermann et al., 2012

Table S2. Properties of somatic and axonal APs in PV^+-BCs during a 1-s high-frequency train at physiological temperature, related to Figure 1.

First AP				
	Peak amplitude	**Half-duration**	**Maximal rise slope**	**Maximal decay slope**
Soma (n = 41)	79.0 ± 1.8 mV	0.22 ± 0.01 ms	705 ± 30 V s^{-1}	388 ± 20 V s^{-1}
Proximal axon [a] (n = 22)	88.7 ± 3.6 mV	0.26 ± 0.01 ms	1014 ± 72 V s^{-1}	352 ± 20 V s^{-1}
Distal axon [a] (n = 14)	82.9 ± 2.4 mV	0.32 ± 0.03 ms	620 ± 63 V s^{-1}	257 ± 26 V s^{-1}
Entire axon (n = 41)	86.4 ± 2.2 mV	0.29 ± 0.02 ms	784 ± 51 V s^{-1}	302 ± 17 V s^{-1}
Last AP				
	Peak amplitude	**Half-duration**	**Maximal rise slope**	**Maximal decay slope**
Soma (n = 36)	57.0 ± 2.7 mV	0.37 ± 0.03 ms	336 ± 36 V s^{-1}	171 ± 21 V s^{-1}
Proximal axon [a] (n = 20)	50.1 ± 5.0 mV	0.53 ± 0.03 ms	283 ± 54 V s^{-1}	119 ± 18 V s^{-1}
Distal axon [a] (n = 12)	62.8 ± 4.4 mV	0.53 ± 0.08 ms	338 ± 40 V s^{-1}	117 ± 13 V s^{-1}
Entire axon (n = 36)	60.0 ± 3.2 mV	0.55 ± 0.03 ms	338 ± 34 V s^{-1}	110 ± 11 V s^{-1}

Recordings were performed at ~35˚C.

Values in Table S2 are presented as median ± SEM.

[a] Boundary between proximal and distal compartment was set at a distance of 100 µm from axon origin.

Table S3. Gating properties and density of Na^+ conductance in PV^+-BC axons, related to Figures 3, 4 and 5.

	Activation	**Deactivation**	**Inactivation**	**Inactivation onset / recovery (prepulses)**
Midpoint potential	−40.1 ± 1.1 mV (n = 14) [a]		−76.5 ± 1.6 mV (n = 13) [a]	
Slope factor	7.4 ± 0.6 mV (n = 14) [a]		7.8 ± 0.2 mV (n = 13) [a]	
τ	230 ± 17 µs at −40 mV (n = 4) [a]	126 ± 8 µs at −40 mV (n = 7) [a]	1.50 ± 0.14 ms at −40 mV (n = 11) [a]	
τ	61 ± 6 µs at 0 mV (n = 4) [a]	46 ± 9 µs at −110 mV (n = 7) [a]	319 ± 21 µs at 0 mV (n = 11) [a]	
τ				16.4 ± 2.2 ms at −70 mV (n = 7)
τ				4.42 ± 1.07 ms at −90 mV (n = 3)
τ				2.70 ± 0.38 ms at −120 mV (n = 5)
$\overline{g_{Na}}$	271.1 ± 32.7 pS µm^{-2} (n = 37) in proximal axon [a] 542.1 ± 120.8 pS µm^{-2} (n = 11) in distal axon [a]			

[a] Median and SEM values were determined from Hu and Jonas, 2014.

Values in Table S3 are presented as median ± SEM.

Table S4. Gating properties and density of K^+ conductance in PV^+-BC axons, related to Figures 3 and 5.

	Activation	**Deactivation**
Midpoint potential	−4.8 ± 5.3 mV (n = 5)	
Slope factor	22.9 ± 3.9 mV (n = 5)	
τ	449 ± 27 µs at 70 mV (n = 5)	4.11 ± 0.83 ms at −40 mV (n = 5)
τ	3.06 ± 0.47 ms at −20 mV (n = 5)	403 ± 23 µs at −130 mV (n = 5)
$\overline{g_K}$	113.1 ± 22.7 pS µm^{-2} in proximal axon (n = 19) 145.1 ± 20.2 pS µm^{-2} in distal axon (n = 11)	

Values in Table S4 are presented as median ± SEM.

Table S5. Hodgkin-Huxley-type model of Na^+ and K^+ channels gating in PV^+-BC axons, related to Figures 5.

Na^+ channels	α_m	β_m	α_h	β_h
A	0.2567 ms^{-1}	0.1133 ms^{-1}	0.00105 ms^{-1}	4.827 ms^{-1}
B	60.84 mV	30.253 mV	-	18.646 mV
C	9.722 mV	2.848 mV	20.000 mV [a]	12.452 mV
K^+ channels	α_n	β_n	$\alpha_{n'}$	$\beta_{n'}$
A	0.0610 ms^{-1}	0.001504 ms^{-1}	0.0993 ms^{-1}	0.1379 ms^{-1}
B	−29.991 mV	-	−33.720 mV	-
C	27.502 mV	17.177 mV	12.742 mV	500.000 mV [a]

$\alpha_m(V) = A\,[-(V+B)] / \{\mathrm{Exp}[-(V+B) / C] - 1\}$ (Eq. 1a)

$\beta_m(V) = A\,(V+B) / \{\mathrm{Exp}[(V+B) / C] - 1\}$ (Eq. 1b)

$\alpha_h(V) = A\,\mathrm{Exp}(-V / C)$ (Eq. 2a)

$\beta_h(V) = A / \{\mathrm{Exp}[-(V+B) / C] + 1\}$ (Eq. 2b)

$\alpha_n(V) = A\,[-(V+B)] / \{\mathrm{Exp}[-(V+B) / C] - 1\}$ (Eq. 3a)

$\beta_n(V) = A\,\mathrm{Exp}(-V / C)$ (Eq. 3b)

$\alpha_n'(V) = A\,[-(V+B)] / \{\mathrm{Exp}[-(V+B) / C] - 1\}$ (Eq. 4a)

$\beta_n'(V) = A\,\mathrm{Exp}(-V / C)$ (Eq. 4b)

[a] At limit of parameter range

Table S6. Parameters of single-compartment model, related to Figure 5.

Parameter	Value	Reference
C_m	9 fF µm^{-2} (0.9 µF cm^{-2})	Nörenberg et al., 2010
g_L	1 pS µm^{-2} (0.1 mS cm^{-2})	
$\overline{g_{Na}}$	500 pS µm^{-2}	Hu and Jonas, 2014
$\overline{g_K}$	150 pS µm^{-2}	Hu et al., 2010; this paper
V_{Na}	+55 mV	
V_K	−90 mV	
V_L	−65 mV	
V_{rest}	−65 mV	
Q_{10} (m, h, and n or n')	2.2, 2.9, 3.0	Schwarz and Eikhof, 1987; Frankenhaeuser and Moore, 1963

Rates (Eq. 1 – 4) were temperature- and offset-corrected before use in simulations (for details, see METHOD DETAILS).

Table S7. Parameters and predictions of detailed cable model, related to Figure 5.

Parameter	Value	Reference
C_m	9 fF µm^{-2} (0.9 µF cm^{-2})	Nörenberg et al., 2010
g_L	1 pS µm^{-2} (0.1 mS cm^{-2})	
R_i	1.7 MΩ µm (170 Ω cm)	Nörenberg et al., 2010
$\overline{g_{Na}}$ (axon)	500 pS µm^{-2}	Hu and Jonas, 2014
$\overline{g_{Na}}$ (soma)	200 pS µm^{-2}	
$\overline{g_{Na}}$ (dendrites)	50 pS µm^{-2}	Hu et al., 2010
$\overline{g_K}$	300 pS µm^{-2}	Hu et al., 2010; this paper
V_{Na}	+55 mV	
V_K	−90 mV	
V_L	−70 mV	
V_{rest}	−70 mV	
Q_{10} (m, h, and n or n')	2.2, 2.9, 3.0	Schwarz and Eikhof, 1987; Frankenhaeuser and Moore, 1963

Rates (Eq. 1 – 4) were temperature- and offset-corrected before use in simulations (for details, see METHOD DETAILS).

Predictions of the model

AP properties				
Compartment	**Peak amplitude**	**Half-duration**	**Maximal rise slope**	**Maximal decay slope**
Soma	81.3 ± 1.5 mV	0.671 ± 0.021 ms	206 ± 15 V s^{-1}	134 ± 4 V s^{-1}
Axon	84.2 ± 4.7 mV	0.400 ± 0.069 ms	475 ± 25 V s^{-1}	240 ± 12 V s^{-1}
Apical dendrite	19.6 ± 2.7 mV	0.667 ± 0.042 ms	59 ± 7 V s^{-1}	49 ± 7 V s^{-1}
Basal dendrite	41.3 ± 8.8 mV	0.626 ± 0.036 ms	104 ± 24 V s^{-1}	101 ± 23 V s^{-1}

Values in Table S7 are presented as median ± SEM.